

Normal Faulting during the August 1989 Earthquakes in Central Afar: Sequential Triggering and Propagation of Rupture along the Dôbi Graben

by E. Jacques,^{*} T. Kidane, P. Tapponnier,[†] I. Manighetti, Y. Gaudemer, B. Meyer,[‡] J. C. Ruegg, L. Audin, and R. Armijo

Abstract In August 1989, an earthquake sequence including ten events with $6.3 \geq M \geq 5.5$ in the first two days produced widespread ground deformation in the Dôbi graben of central Afar. Numerous surface breaks with complex geometry, including fresh scarplets with vertical throws up to 30 cm high and open fissures up to 30 cm wide, were observed. Coseismic slip incremented the deformation (normal faulting, block tilting, and counterclockwise rotation of basaltic slices) accumulated in the last 2 m.y. in the transfer zone between the Dôbi and Hanle grabens. By combining maps of surface ruptures, relative event relocations with the local Djibouti network, published focal mechanisms, and source sizes, we tentatively relate most of the mainshocks of the sequence to slip on individual faults. The largest shocks at 11h16 on 20 August 1989 (M_S 6.2) and at 1h09 on 21 August 1989 (M_S 6.3) ruptured southern segments of the southwestern bounding fault of the graben. A dozen other faults also slipped along the edges of, and inside, the graben. On average, triggered seismic faulting propagated about 35 km northwestward along the graben in about 20 hr. Slip on the main faults was coupled with slip on secondary antithetic faults branching from them at depth. Although the Dôbi earthquakes ruptured part of the fault array between the Asal rift (1978 sequence) and the Serdo region (1969 sequence), an approximately 50-km-long gap subsists along the Der'êla half-graben. We infer the patterns of surface faulting in the Dôbi sequence, which coinvolved bookshelf-faulting about both horizontal and vertical axes, to typify the complexity of coseismic stress release in central Afar and in other active zones of distributed extension (e.g., Iceland, Abruzzi, Basin and Range).

Online Material: Additional photos and descriptions of surface effects of the Dôbi earthquake sequence.

Introduction

On 20 August 1989, a seismic sequence started within central Afar with a strong earthquake (11h16 UTC, M_S 6.2), followed in the next 50 hr by 17 events with $5.0 < M < 6.3$. This was the largest earthquake sequence in the Afar triangle since the March–April 1969 Serdo sequence, which also included several events with comparable magnitudes (McKenzie *et al.*, 1970; Gouin, 1979; Kebede *et al.*, 1989), and prior to the Manda Hararo/Dabahu rifting episode in

northern Ethiopia (about 20 events with $5.0 \geq M \geq 5.4$ in 12 days; Wright *et al.*, 2006; Ayele *et al.*, 2007; Rowland *et al.*, 2007; Ebinger *et al.*, 2008; Grandin *et al.*, 2009; Ayele *et al.*, 2009). Sequences of large earthquakes clustered in a few days appear to typify the tectonic stress release in much of Afar and may be common also in other regions of distributed extension. It is thus important to understand the processes that lead to this peculiar mode of elastic-strain release.

On a regional scale, a bookshelf tectonic model accounts for brittle deformation distributed on northwest-southeast striking normal faults between two overlapping, active volcanic rifts (Manda Inakir-Asal and Manda Hararo Goba'ad rifts, abbreviated MI-A and MHG; Fig. 1; Tapponnier *et al.*,

^{*}Previously at Ecole et Observatoire des Sciences de la Terre, UMS 830-EOST, Strasbourg, France.

[†]Also at Tectonic Group, Earth Observatory of Singapore, Nanyang Technological University, Singapore.

[‡]Also at CNRS, ISTEP, UMR 7193 CNRS, Paris, France.

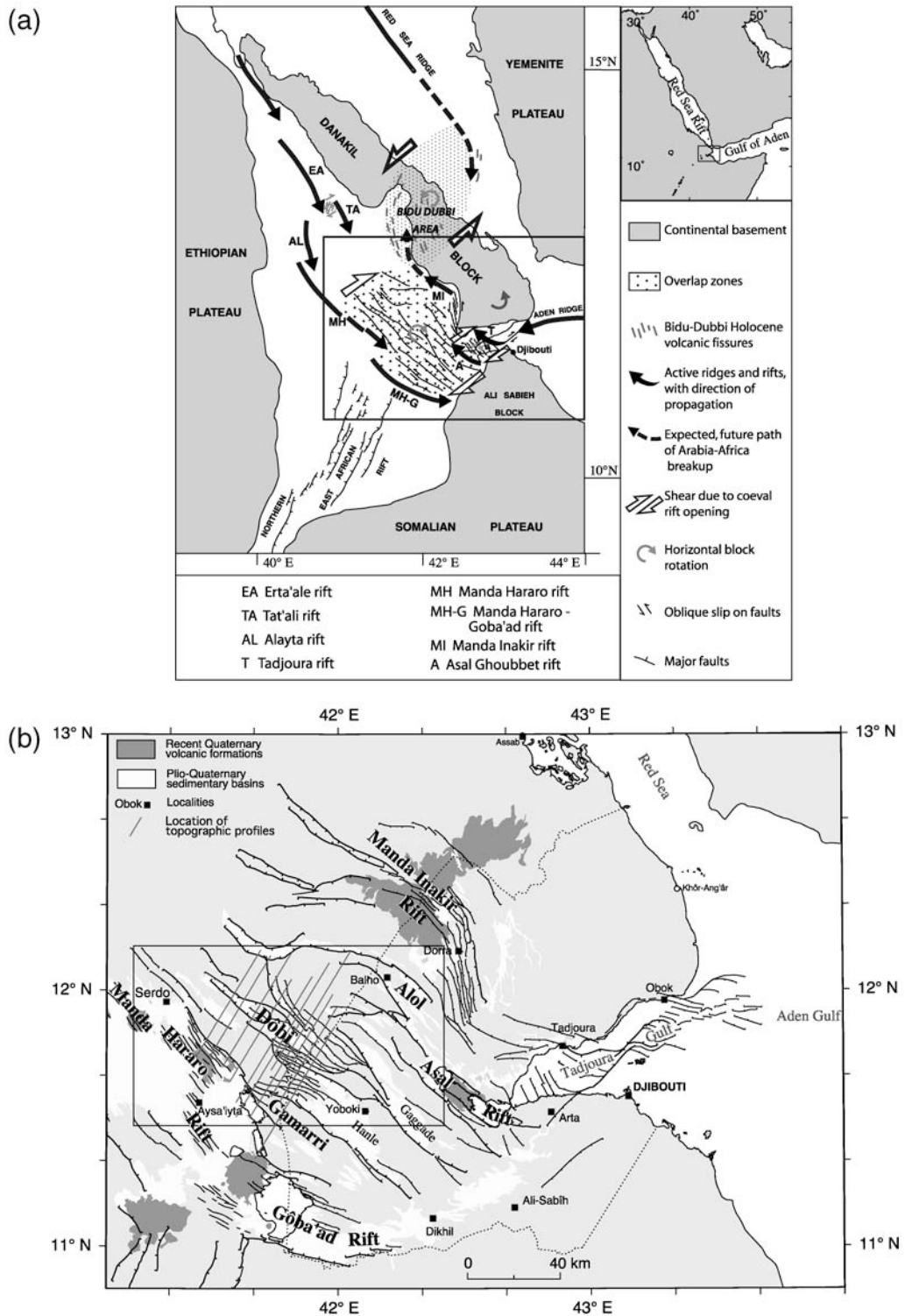


Figure 1. (a) Tectonic model of Afar depression with propagating rifts (redrawn from [Manighetti et al., 2001](#)). Inset is location of Figure 1 along Gulf of Aden-Red Sea rift. Boxes show frame of Figure 1b. (b) Tectonic setting of Dôbi graben within Central Afar bookshelf-faulting zone. Quaternary faults redrawn from [Varet and Gasse \(1978\)](#), [Consiglio Nazionale delle Ricerche and Centre National de la Recherche Scientifique \(1975\)](#), and [Manighetti \(1993\)](#). Box shows frame of Figure 3a.

1990; note also the microplate model of [Acton et al., 1991](#)). Strain transfer between the two rifts zones, which accommodate most of the divergent motion between the Arabian and African plates, induces right-lateral shear, causing clockwise

rotations of the northwest-southeast trending crustal blocks in between. The normal faults bounding these crustal blocks are thus presently activated with a significant component of left-lateral motion. This model is in keeping with both field

observations (Manighetti, 1993 and Manighetti *et al.*, 2001), earthquake mechanisms solutions (McKenzie *et al.*, 1970; Kebede *et al.*, 1989; Lépine and Hirn, 1992), and measured clockwise paleomagnetic block rotations ($14^\circ \pm 7^\circ$; Courtillot *et al.*, 1984) within the overlap. An improved bookshelf model (Sigmundsson, 1992), taking into account residual extension between the two rift zones (10% to 20% of the total according to Manighetti [1993] and Manighetti *et al.* [2001]), is corroborated by predominant normal faulting during the 1989 events (Braunmiller and Nabelek, 1990; Dziewonski *et al.*, 1990). Fault kinematics and paleomagnetic studies (Manighetti, 1993; Manighetti *et al.*, 1998; Manighetti *et al.*, 2001) imply that the overlap zone has grown in the last 200 k.y. by propagation of the Aden ridge from the Asal to the Manda Inakir rift, adding to the initial overlap a region affected by smaller clockwise rotation (Manighetti, 1993; Manighetti *et al.*, 2001). The two parts of the overlap are separated from each other by the Gamarri-Alol tear or segmentation zone, the former northwestern edge of the initial overlap and possible northernmost extension of the East African rift (Fig. 1).

The Dôbi earthquake sequence occurred mainly along the Dôbi graben and partly in the Gamarri-Alol segmentation zone (Fig. 1; Jacques, 1995; Jacques *et al.*, 1999). In this paper, we document the geometry and kinematics of surface ruptures observed and/or measured in the field during several field trips. The main goal was to understand how seismic motions during the Dôbi sequence triggered one another and incremented the longer-term deformation (2 m.y. time-scale). For this, we combined different data sets: an analysis of surface ruptures, coupled with a specific 3D tectonic study of the Dôbi graben, the epicentral relocations obtained using the Djibouti seismological network (Jacques, 1995; Jacques *et al.*, 1999), and the focal mechanisms of the $m_b > 5$ events (Braunmiller and Nabelek, 1990; Dziewonski *et al.*, 1990).

Overall Geometry of Regional Quaternary Faulting

The Kadda Dôbi graben (Fig. 2; hereafter referred to as the Dôbi graben) is located in the central Afar depression, northeast of the southern termination of the Manda Hararo rift (Fig. 1). It is the right-stepping northwestern continuation of the Hanle and ϵ ounda Dôbi half-grabens. Laterally, it is connected to the Immino graben through the Gumma graben. It forms a wedge-shaped trough that widens southeastward into the Gamarri-Alol zone (Figs. 1 and 3a) and is partly filled with lacustrine Holocene sediments, which are locally faulted (Rognon and Gasse, 1972).

The combined analysis of topographic maps, aerial photographs, and satellite images provides insight into the 3D structure of this graben (Fig. 3b,c). It is bounded by three main normal faults: *D1* and *D2* dipping northeast to the southwest and *D3* dipping southwest to the northeast. The cumulative vertical throws of the main antithetic fault systems decrease southeastward. Consequently, where *D1* and *D3* reach the Gamarri-Alol zone, they become hardly distinguishable from the numerous, smaller normal faults that characterize this zone. The southwest-dipping normal fault *D4* cuts the graben floor in its central part, merging with *D3* near its southeastern end. As the northwestern stretch of *D1* (*D1b*) enters the Gamarri-Alol zone, its $\sim N130^\circ E$ -striking trace veers 50° in a more northerly direction. The sections of *D1* west and east of its pronounced kink are dubbed *D1a* and *D1b*, respectively. While *D1b* consists of one fault segment, *D1a* splits into several segments. A southwest-dipping fault (*D5*) runs parallel to *D1* to the southeast, bounding to the north the ϵ ounda Dôbi half-graben termination (Fig. 3). To the southeast, *D3* gives place to other southwest-dipping faults (*K1b* and *K1a*) and to a northeast-dipping fault (*K2*), which together bound the Kambourta graben (Fig. 3).

Northwest of the *D1* kink, the number of faults decreases, whereas their apparent vertical throws increase (northwest of profile 5, Fig. 3a,b). The whole Dôbi graben exhibits an asymmetric structure with greater throw on *D1* to



Figure 2. Southeast-looking view of southeastern part of Dôbi graben (April 1994) from road descending along southwestern graben flank. View of tilted basaltic slices at southeastern end of *D1b*.

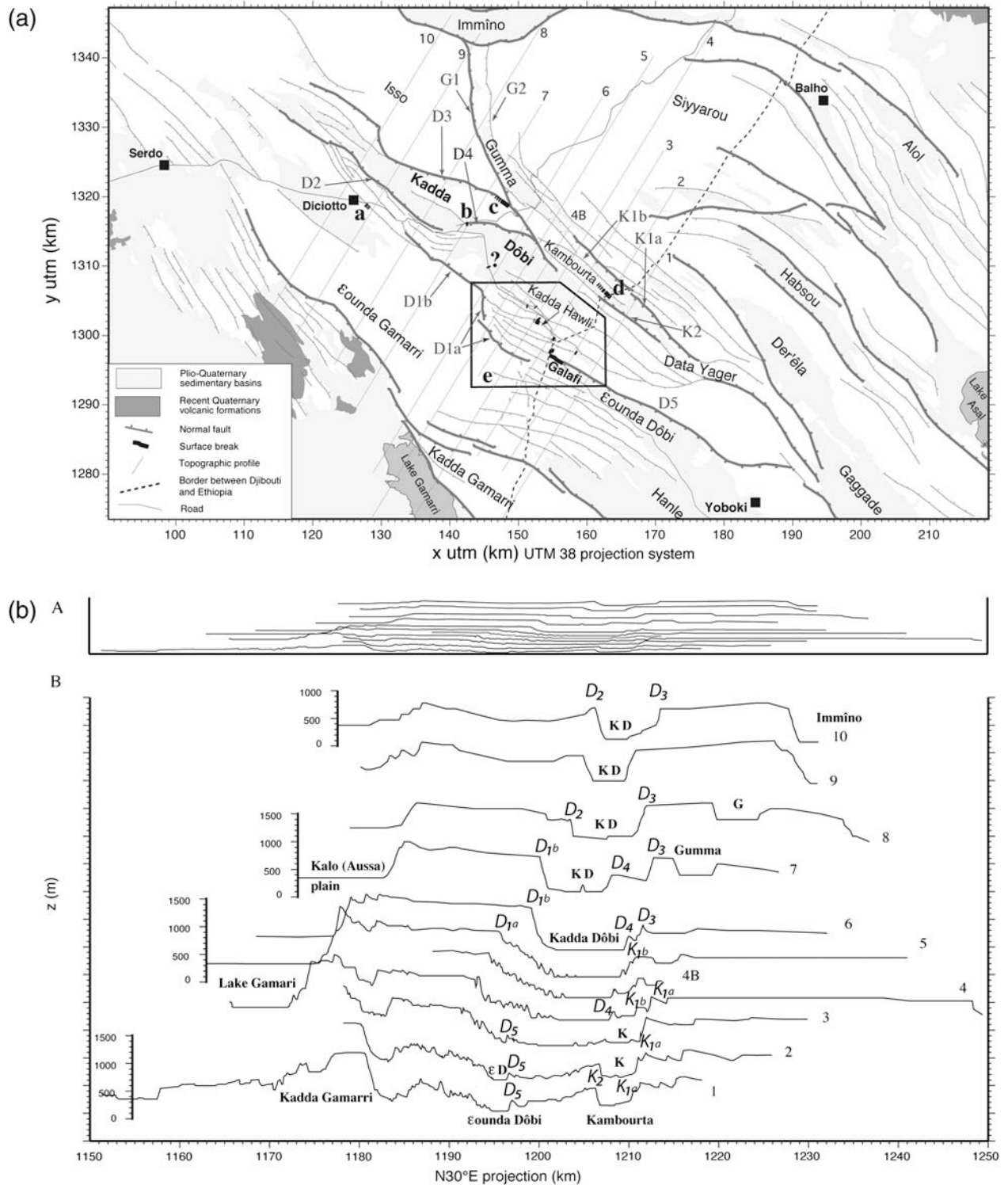


Figure 3. (a) Seismotectonic map of Dôbi graben region where August 1989 earthquake sequence occurred. Sites identified by letters a–e are where surface ruptures were observed, dashed lines are topographic profiles (P1–P10) shown in Figure 3b. Small box e indicates Galafi–Kadda Hawli region. Symbol “?” refers to ambiguous surface rupture. (b) N30°E-striking topographic profiles 1–10 across Dôbi graben. A: no vertical exaggeration, B: with vertical exaggeration of 8. Profiles 1 to 6 were digitized from Abhe and Gamarri maps from the [Institut Géographique National \(1953\)](#) (contour interval 25 m, scale 1/100,000). Profiles 7 to 10 were digitized from the maps of Urikomam-Terara and Serdo-French Territory of Afar and Issas ([Ethiopian Mapping Agency, 1979](#); contour interval 100 m, scale 1:250,000). Profiles 4 to 6 were complemented in their most northeastern part with EMA maps. Central part of profile 7 was derived from the Gamarri map. Though profile subsets have variable accuracy, they show overall structure of Dôbi (Kadda Dôbi) and adjacent grabens, as the Eounda Dôbi half-graben, Gumma graben, and Kambourta graben, identified by letters KD, εD, G, and K, respectively. (c) Schematic 3D bloc-diagram of Dôbi graben region deriving from Figure 3a,b. (Continued)

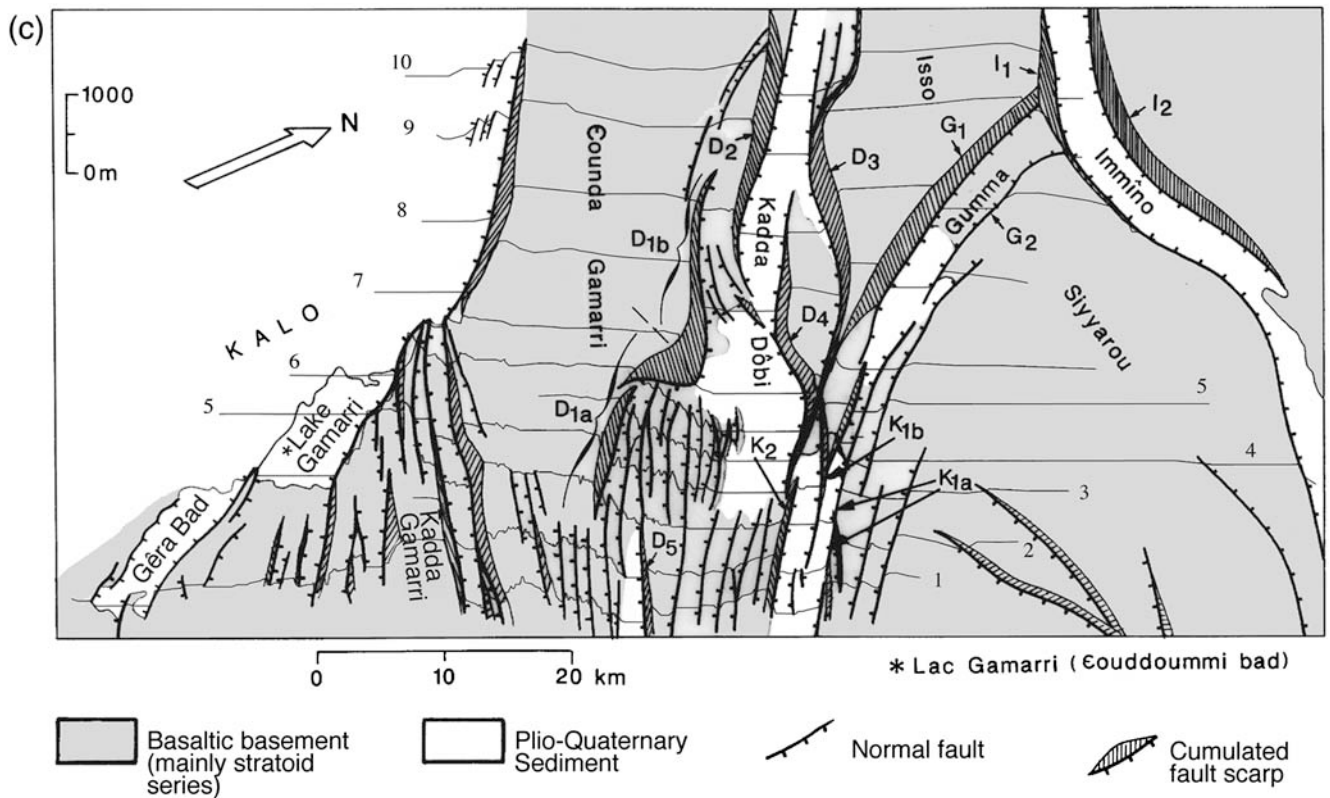


Figure 3. Continued.

the southeast (reaching up to 750 m west of its kink) and on the antithetic $D3$ fault to the northwest (~ 570 m). The change in maximum throw distribution as a function of fault dip occurs in the central part of the graben, between profiles 7 and 8 (Fig. 3b,c). The stepping geometry of the Dôbi graben border suggests that they move with a slight component of left-lateral strike-slip. See, for instance, the right-stepping arrangement of an échelon faults $D1$ and $D2$ and the rhomb-shaped, pull-apart-type connection between $D3$ and $D4$ (dipping southwest) and $D3$ and $D2$, through $D4$.

The εounda Gamarri plateau is tilted northeastward by 0.2° – 0.7° , southwest of the Dôbi graben (topographic profiles 5 to 8, Fig. 3b,c). The Isso block, by contrast, is tilted southwestward by 0.5° (profiles 9 to 10). Such tilts are antithetic to those expected from faulting along the graben. The mean level of the Kalo (or Aussa) plain is ~ 230 m higher than that of the Dôbi graben floor (profiles 4 to 8 and 10, Fig. 3b,c). This is due to sediment deposition by the Awash River, while the internally drained Dôbi trough is starved from such infilling. The floor of the even more isolated Immîno graben lies ~ 50 m lower than the Dôbi graben. The floor of the Gumma graben, on the other hand, is perched ~ 300 m higher than Immîno and Dôbi (profiles 8 to 10), which can only be caused by less tectonic subsidence.

Most of the seismic surface breaks found were located in the Galafi–Kadda Hawli region of the southeastern Dôbi graben (20×15 km², small box in Fig. 3a). This area, on the

hanging wall of the southern termination of $D1$, west of its kink, is affected by three kinds of Quaternary faults, which control the brittle deformation.

Hierarchically, there are two main first-order faults, $D1$ and $D5$. $D1a$ is a left-lateral array of four distinct, right-stepping segments, 2–4.5 km long (Figs. 3 and 4). Their surface dips average 70° , and their minimum cumulative throws vary between 150 and 750 m. Where the surface trace of $D1$ is interrupted, for a distance of about 1 km, ~ 3 km south of the kink, there is continuity between the εounda Gamarri plateau footwall and some of the hanging-wall tilted blocks (between profiles 5 and 6, Fig. 4c). South of the kink, the mean strike of $D1a$ rotates counterclockwise from $N175^\circ E$ to $N125^\circ E$. $D5$ exhibits a linear trace, 45 km long, whose strike veers slightly westward from $N130^\circ E$ to $N115^\circ E$. Its minimum vertical throw decreases from ~ 600 m, 20 km southeast of the Djibouti–Ethiopia border, to only a few tens of meters where it faces $D1a$ (profiles 1 to 4, Fig. 4a–b). The westernmost, $\sim N115^\circ E$ striking, 10-km long section of $D5$ is therefore barely distinguishable from the smaller, mostly south–southwest dipping faults of the area, which are dubbed second-order faults.

These second-order faults, mostly antithetic to $D1a$, govern the structure and morphology of the southwestern border of the graben, west of Galafi. They strike $N100^\circ E$ to $N110^\circ E$, north of Galafi, and between $N110^\circ E$ and $N120^\circ E$ to the south (Fig. 4b). They are 5–9 km long, with

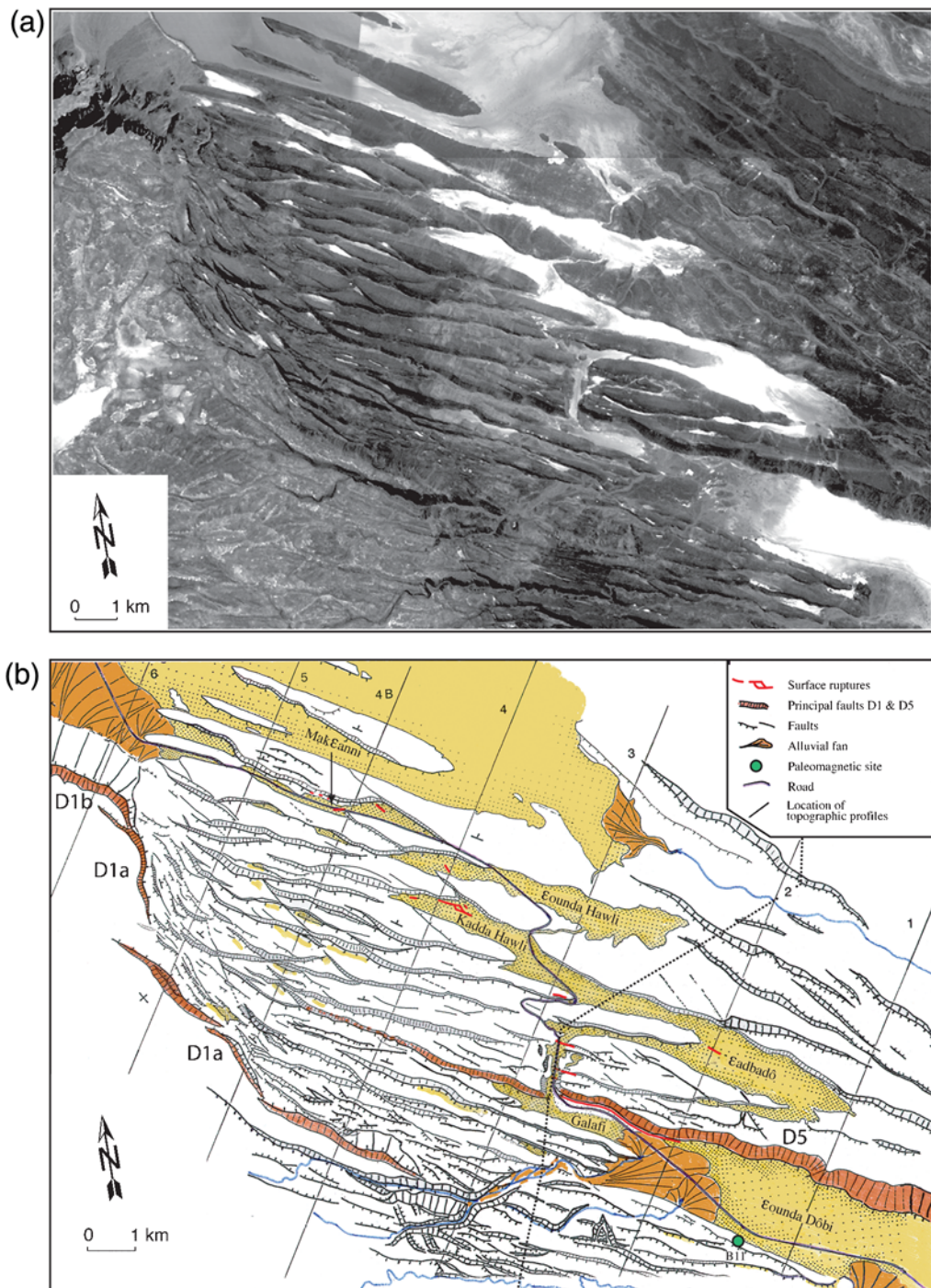


Figure 4. (a) Spot image mosaic of Galafi–Kadda Hawli region. (b) Tectonic and geological interpretation of Figure 4a; locations of topographic profiles are indicated; Djiboutian–Ethiopian border is a dotted line. (c) Tectonic and geological interpretation of profile sections in Figure 4b. Stars indicate faults with observed seismic rupture. (Continued)

south–southeast-facing escarpments and vertical throws ranging between ~20 m and ~150 m. They cut piles of northeast-dipping basaltic flows (stratoid series, locally 2 ± 0.2 m.y. old; Courtillot *et al.*, 1984; Kidane *et al.*, 2003) into regular slices 0.5–1.5 km wide, most of them tilted northeastward by $15^\circ \pm 5^\circ$ (Fig. 4c). They join *D1a* in a fault termination pattern dubbed rudder tail (Jacques, 1995), with *D1b* being the rudder

handle (Fig. 5a). This surface pattern reflects the 3D deepening of antithetic fault-plane intersections with *D1*, but is similar to a 2D left-lateral horse-tail termination (e.g., Granier, 1985; Manighetti, 1993). It implies a left-lateral slip-component on the $N125^\circ E$ and $N165^\circ E \pm 5^\circ$ striking segments of *D1b* and *D1a*. Westward, the second-order faults veer clockwise by 20° – 40° before meeting with *D1a*.

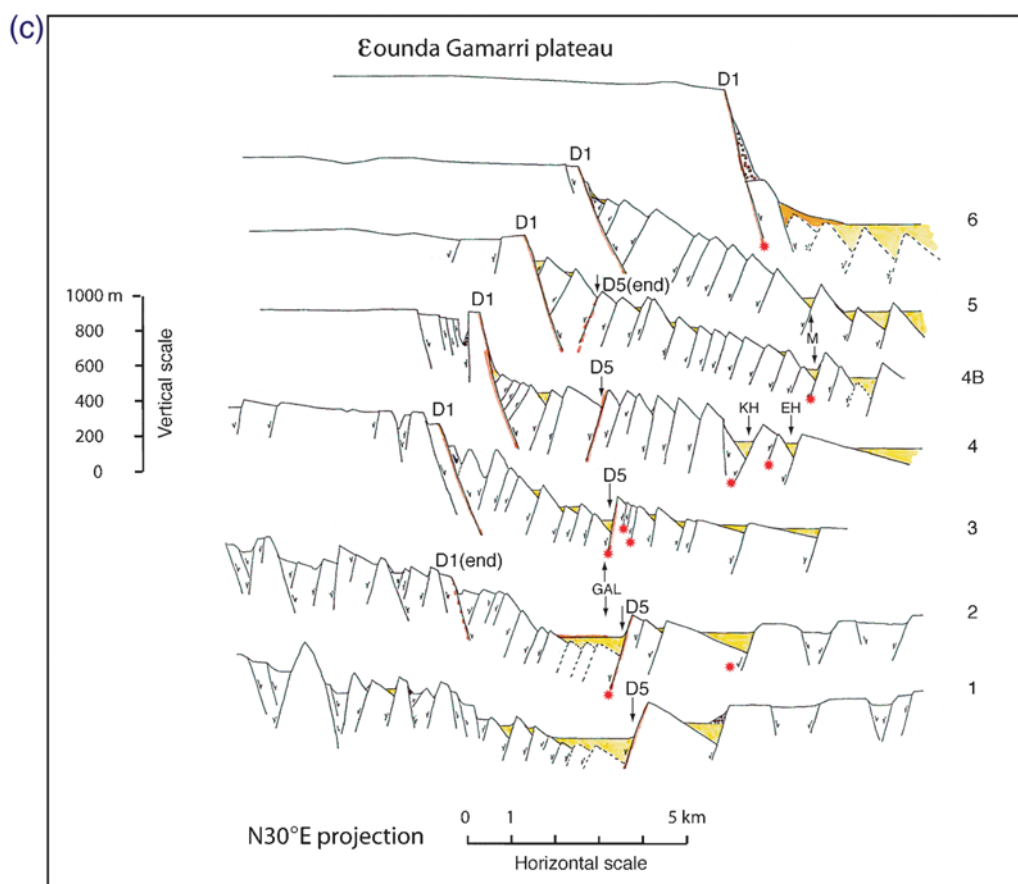


Figure 4. Continued.

This strike change is accompanied by the development of $N150^{\circ}E \pm 20^{\circ}$ striking, third-order faults (Figs. 4b and 5a).

These 0.3–1.5 km long third-order faults cut the tilted basaltic slices bounded by the second-order faults and sometimes crosscut the latter. The third-order faults generally have the smallest vertical throws. Some are just open fissures (Fig. 4b). They strike between $N170^{\circ}E$ and $N140^{\circ}E$ near *D1a* and between $N135^{\circ}E$ and $N115^{\circ}E$ farther east. Where they connect with the second-order faults, they generally do so through slight counterclockwise bends and with dextral horsetail terminations. Locally, some third-order faults also tend to form dextral en échelon arrays parallel to the second-order faults (Figs. 4b and 5a). Such patterns are consistent with a right-lateral component of movement along the second-order faults. At the same time, the northerly striking third-order faults tend to form sinistral en échelon arrays along and near the trace of *D1a*. Overall, such small, conjugate-lateral slip components imply that the minimum horizontal principal stress σ_3 in the Galafi–Kadda Hawli area is oriented about $N30^{\circ}E$ (Fig. 5a). The stress σ_3 possibly strikes more easterly close to *D1*, and, given the strike change of the third-order faults, more northerly farther east or north (Fig. 5a).

In any case, the long-term deformation analysis requires oblique normal, right-lateral slip on the $N110^{\circ}E$ -striking

second-order faults. The absence of systematic crosscutting relationships between the different fault sets imply that they are all coevally active, even though the third-order, more northerly striking faults with the smallest throws appear to be the youngest. They probably accommodate diffuse, minor deformation within the $\sim N110^{\circ}E$ -trending basaltic slices and help facilitate the displacement of these slices relative to their neighbors.

The sections in Figure 4c depict the structural relationship between the different fault sets. Although the vertical throw of *D1* decreases from 750 m (profile 6) to 100 m (profile 2), the elevation difference between the ϵ ounda Gamarri plateau (800–900 m) and the Dôbi graben floor (100–150 m) remains nearly constant. On section 6, the steep relief results mainly from throw on *D1*. In sections 2–5 by contrast, there is a more gradual transition due to slip distribution on the numerous second-order faults. The altitudes of the tilted blocks decrease regularly northeastward, while their widths tend to increase. There are several perched, isolated sedimentary basins between the blocks (Fig. 4c). The cross sections imply that the second-order faults join at depth with the main *D1* fault plane, whose dip must then decrease with depth, a listric geometry, but without rollover hanging-wall back tilt. Figure 4c in fact shows that where the ϵ ounda Gamarri plateau divides into many smaller blocks,

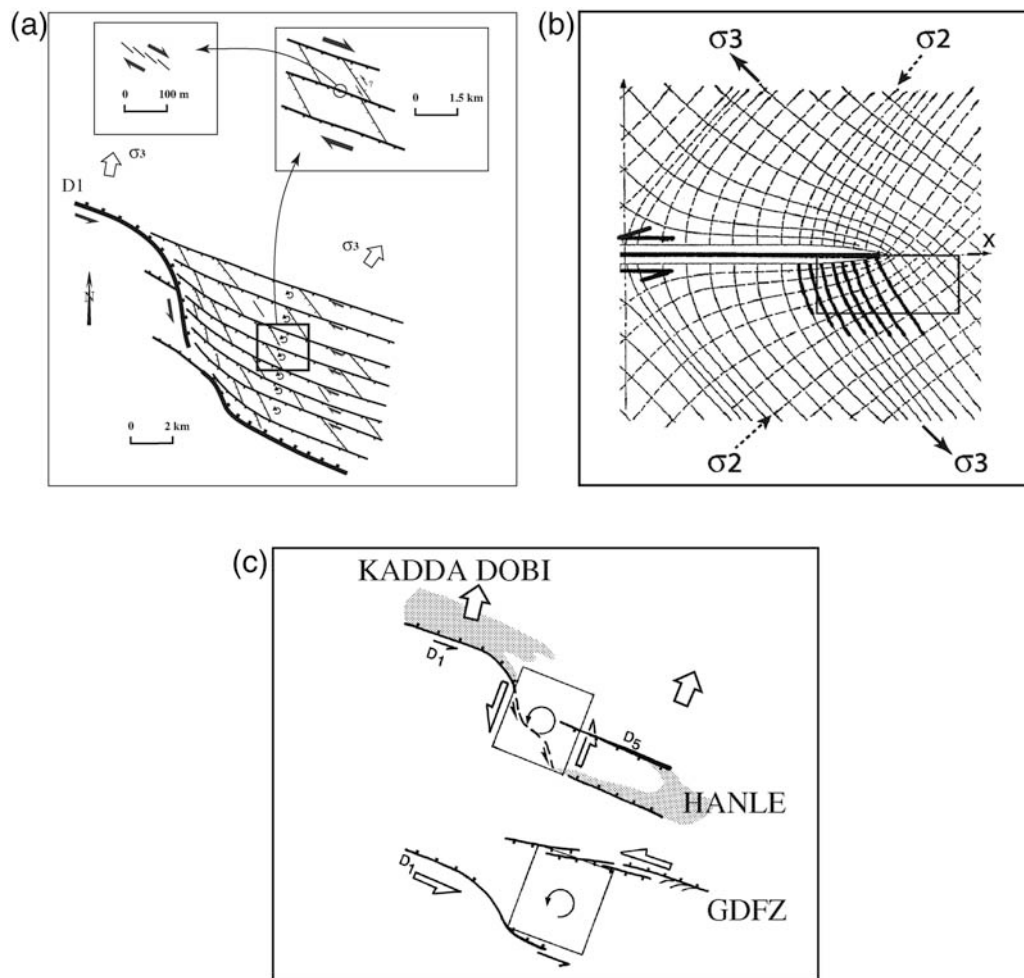


Figure 5. (a) Hierarchy of deformation mechanism in Galafi–Kadda Hawli region. (b) Stress changes induced by left-lateral strike-slip faulting (from Xiaohan, 1983). Fault, bold line, is modeled as weak zone in elastic medium under northeast striking, regional maximum horizontal stress (σ_2) compatible with motion. Dotted lines are trajectories of σ_2 , continuous lines of minimum horizontal stress (σ_3). Small box shows a zone whose location relative to modeled fault is similar to that of Galafi–Kadda Hawli region relative to D1. Note that in this box, clockwise rotation of local σ_3 (small thick continuous lines) relative to regional, southeast striking σ_3 . (c) Two kinematic models accounting for deformation of Galafi–Kadda Hawli region (small box), (upper part of c) due to bookshelf faulting related to counterclockwise rotation resulting from kinematic transfer between right-stepping Hanle–εounda Dôbi and Kadda Dôbi grabens, (lower part of c) due to left-stepping diffuse transfer of left-lateral strike-slip-component from Gaggade-Der'êla fault zone (GDFZ) to Dôbi fault D1.

D1 terminates southward into a large flexure with block rotations about horizontal axes nearly orthogonal to the N30°E direction (vertical bookshelf faulting).

The Dôbi Earthquakes and Related Seismic Surface Breaks

Tectonic and Surface Effects of the Earthquakes

The 1989 Dôbi earthquake sequence was strongly felt in a large region straddling the Ethiopia–Djibouti border (see descriptions in Appendix A).

During the sequence, the Dôbi graben floor was flooded (a thin layer of water is mentioned by people living in the Dôbi region). Other examples of widespread water outflow after normal-fault earthquakes are well known (e.g., Hebgen Lake, 1959; Borah Peak, 1983; Muir-Wood and King, 1993).

Hence, right after the events, it was probably difficult to see evidence for surface rupture within the central floor of the graben, which is also filled with unconsolidated lacustrine sediments.

Where it crosses the Dôbi graben, the Addis Ababa–Assab national highway was interrupted by numerous rock slides (reports from the Addis Ababa Observatory). In the central part of the graben, the road to the Galafi, Djibouti, checkpoint was heavily damaged by the opening of fissures (“?” in Fig. 3a), ~7 km south-southeast of its junction with this highway and ~250 m south of a tilted, south-southeast trending block.

On several field trips (two of them 4 and 5 yr after the sequence), we were able to document and map geological surface ruptures resulting unambiguously from the earthquakes in five different areas identified by letters a to e in Figure 3a.

In August 1989, during a helicopter trip northwest of the Ethiopian border, a ≥ 2 km-long zone of N115°E–N130°E-striking fissures 20–50 cm wide and 50–60 cm deep, some with vertical throws ranging between 5 and 30 cm, was observed in the middle of the Kambourta graben floor (**d** in Figs. 3a and 6). They formed a left-lateral en échelon array trending \sim N130°E on average, nearly parallel to the graben bounding faults.

In October 1989, two months after the sequence, the only surface ruptures we could reach in the field were on the Djiboutian side of the border, near Galafi (southeast part of the Galafi–Kadda Hawli region, Figs. 4 and 7a). These ruptures included scarplets along the base of the *D5* fault scarp, N110°E–N130°E-striking, open fissures forming en échelon arrays, and scarplets in sediments (Fig. 7b), as in the ϵ adbado half-graben (Fig. 4b), 4 km east of Galafi, often at the base of meters-high cumulative fault scarps (Manighetti, 1993; Jacques, 1995).

In February 1993, we discovered other well-preserved ruptures in one of the numerous small half-grabens (Kadda Hawli half-graben, Figs. 4b and 8) of this same area, 9 km

east of the *D1* kink. The Galafi–Kadda Hawli ruptures are remarkable enough to justify a separate, detailed description (see Appendix B). We also found open fissures on one foot-wall top, parallel to the cumulative scarp of a second-order fault near the Ethiopian border checkpost (~ 2 km north of Galafi). During the same trip, we found evidence of poorly preserved surface breaks on the western shoulder of the Dôbi graben not far from Diciotto, about 5 km northwestward from the western end of *D1* (**a** in Fig. 3a). These breaks consisted of \sim N120°E trending fissures with blunt edges across alluvium and light-colored exhumation traces caused by stone displacements at the base of a small, south-facing, \sim N135°E-trending fault scarp. Both could be followed discontinuously for ~ 1 km. We also observed several 1–2 m wide mud volcanoes in the same area.

That same year, we were finally able to reach the part of the road between Galafi and the Addis-Assab highway that was fissured most strongly in 1989 (“?” in Fig. 3a). There, we indeed observed fissures meters to tens-of-meters long in an 80 m-long zone, striking \sim N160°E, nearly parallel to the road and to the local trend of third-order faults. The fissures opening ranged between 5 and 10 cm. At the southeastern end of the zone, they were localized between the embankment and the asphalt and formed a left-lateral en échelon array. The longest fissures, which stopped road traffic at the time, reached widths of several tens of centimeters shortly after the earthquakes and were filled with stones. Because the road stands above the graben floor, it remains unclear whether all the fissures were caused by seismic faulting or by shaking and compaction of the embankment. Nevertheless the stone-filled ones were likely too large to reflect only lateral spreading of the road, and it must be emphasized that not all the uplifted road tracts were fissured.

In 1993–1994, about 2 km northwest of the tip of the wedge formed by *D3* and *G1*, we found evidence of clear reactivation of the *D3* cumulative scarp (**c** in Fig. 3a). At the base of the 4–7 m high *D3* free face (Fig. 9), a light-colored scarplet 2 km long, ~ 40 cm high (Fig. 10) marked the top of the scree wedge. The smooth 1–2 m high, lowest and steepest part of that free face, which dips 70°–75° southwest, exposes crushed bedrock cut by small subvertical fissures. It bears slickensides with a pitch averaging 80° SE (Fig. 10b), consistent with a predominant component of normal slip and a small component of left-lateral strike-slip. The ~ 40 cm high, light-colored scarplet (due to the exhumation of underground calcareous crust that weathers to gray-brown with time) is typical of recent seismic faulting, as is well documented in Afar and elsewhere (e.g., Abdallah *et al.*, 1979; Tapponnier *et al.*, 1990; Manighetti, 1993; and Manighetti *et al.*, 2001; Daeron *et al.*, 2005; fault ribbons in the Abruzzi; e.g., Piccardi *et al.*, 1999).

In April 1994, several hundred meters southeast of the highway on the Dôbi graben floor and along the base of the kink of the *D4* cumulative scarp (**b** in Fig. 3a), open fissures were still partly flooded. These N70°–75°E-trending fissures were 5–10 m long and several tens-of-centimeters wide

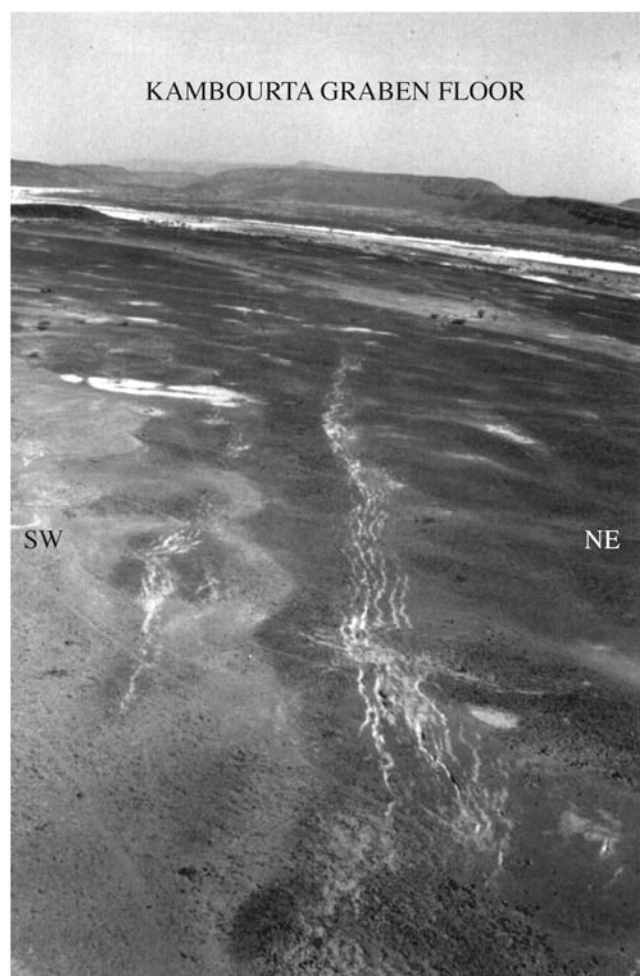


Figure 6. Northwest-looking view, from helicopter, of surface breaks in middle of Kambourta graben floor (**d** in Fig. 3a).

(*D4* strikes \sim N90°E locally). The fissure closest to the road was reported by the inhabitants to have been associated with a hot spring shortly after the earthquakes. Finally, we mapped surprisingly fresh surface breaks in the Makεanni half-graben 2 km northwest of Kadda Hawli (Ⓔ see the electronic supplement to this paper).

The number of distinct observation sites suggests that many of the second-order faults ruptured during the sequence. Some third-order faults were also activated, with well-preserved surface breaks in the εounda Hawli half-graben, in the western part of the Makεanni half-graben (Fig. 4b, Ⓔ see the electronic supplement to this paper), and in the εadbado depression.

Kinematics and Origin of the Surface Breaks at Kadda Hawli

Based on the precise measurements and observations reported in Appendix B, we discuss here in detail the mechanics of faulting at Kadda Hawli because they illustrate well the interaction between multiple coeval fissures in basement and sediments. The fact that most surface breaks formed at some distance from the cumulative scarps suggests a systematic, unusual link between surface rupture and seismic faulting at depth. The relationship between topography, block tilting, faulting, and 1989 seismic slip may be assessed from an \sim 1 km long N15°E-striking, topographic profile (Fig. 11a) leveled across the Kadda Hawli half-graben, perpendicular to *F1* (Fig. 8) and passing through area 3 (Fig. 8, box 3), where the density of measurements is greatest (Appendix B). The profile shows the flat-top surface of block

C tilted $16 \pm 1^\circ$ northeastward, the horizontal flat floor of the half-graben, a result of Holocene infilling by a wedge of lake beds (shaded gray, Fig. 11a), the steep, $39^\circ \pm 1^\circ$ SW-dipping free face of *F1* and the tip of block *A*, which is tilted northeastward by less than 7° .

The fissures in area 3 lie \sim 60 m south of *F1* and \sim 350 m north of block *C* (Fig. 8). The opening of such fissures must result from seismic slip on *F1*. At depth, below the tilted, lakebed/basalt interface, seismic slip occurred on the *F1* fault plane. We infer that the interface between the basaltic basement and the weak Holocene lacustrine beds caused slip refraction (Fig. 11b), so that fissures propagated near-vertically to the surface from the intersection between *F1* and the basement-sediment interface. This accounts for the lack of a fresh rupture along the base of the *F1* cumulative scarp north of area 3. A comparable slip partitioning mechanism operates in Tibet along normal faults with a component of strike-slip (e.g., Armijo *et al.*, 1986) and was recently observed during the 2001 Kokoxili earthquake (Van der Woerd *et al.*, 2002; King *et al.*, 2005; Klinger *et al.*, 2005). It may have occurred along the west side of the Fucino basin on occasion of the 1915 Avezzano earthquake (Voragine, the 1915 fault scarp created by the 1915 Avezzano earthquake; e.g., Ward and Valensis, 1989; Michetti *et al.*, 1996; Galadini *et al.* 1999; Piccardi, 1999).

This interpretation is consistent with a maximum lacustrine limestone thickness of \sim 100 m and with a dip of $52^\circ \pm 1^\circ$ SW for *F1*. If the refracted fissure were not vertical, it could not have dipped less than \sim 65°, because the dip of *F1* cannot be less than its maximum scarp dip ($39^\circ \pm 1^\circ$, Fig. 11a). On the other hand, the present dip of *F1* cannot

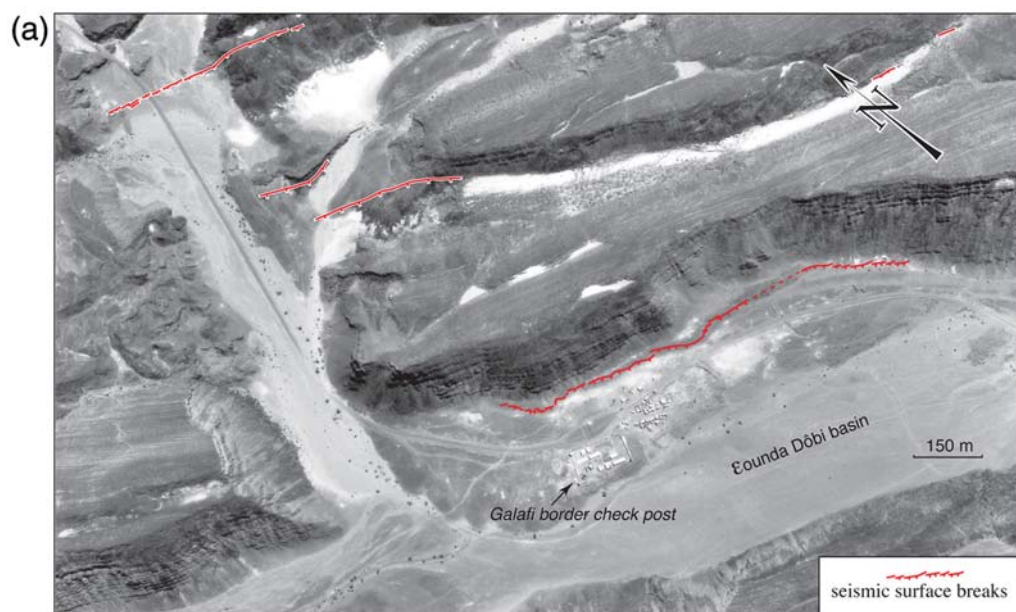


Figure 7. (a) Location and geometry of surface ruptures mapped near Galafi, Djibouti (extract of IGN aerial photo). (b) 1: North-looking view of one eastern Galafi rupture stretch. 2: Map of eastern Galafi ruptures leveled with total-station (point spacing varied from 1 to 5 m). 3: kinematic interpretation: normal fault segments form en échelon array with mean N135°E trend, implying a left-lateral component of motion on N135°E-striking fault segments. (c) Geometry of western Galafi ruptures. 7a, b, and c are redrawn from Manighetti (1993). (Continued)

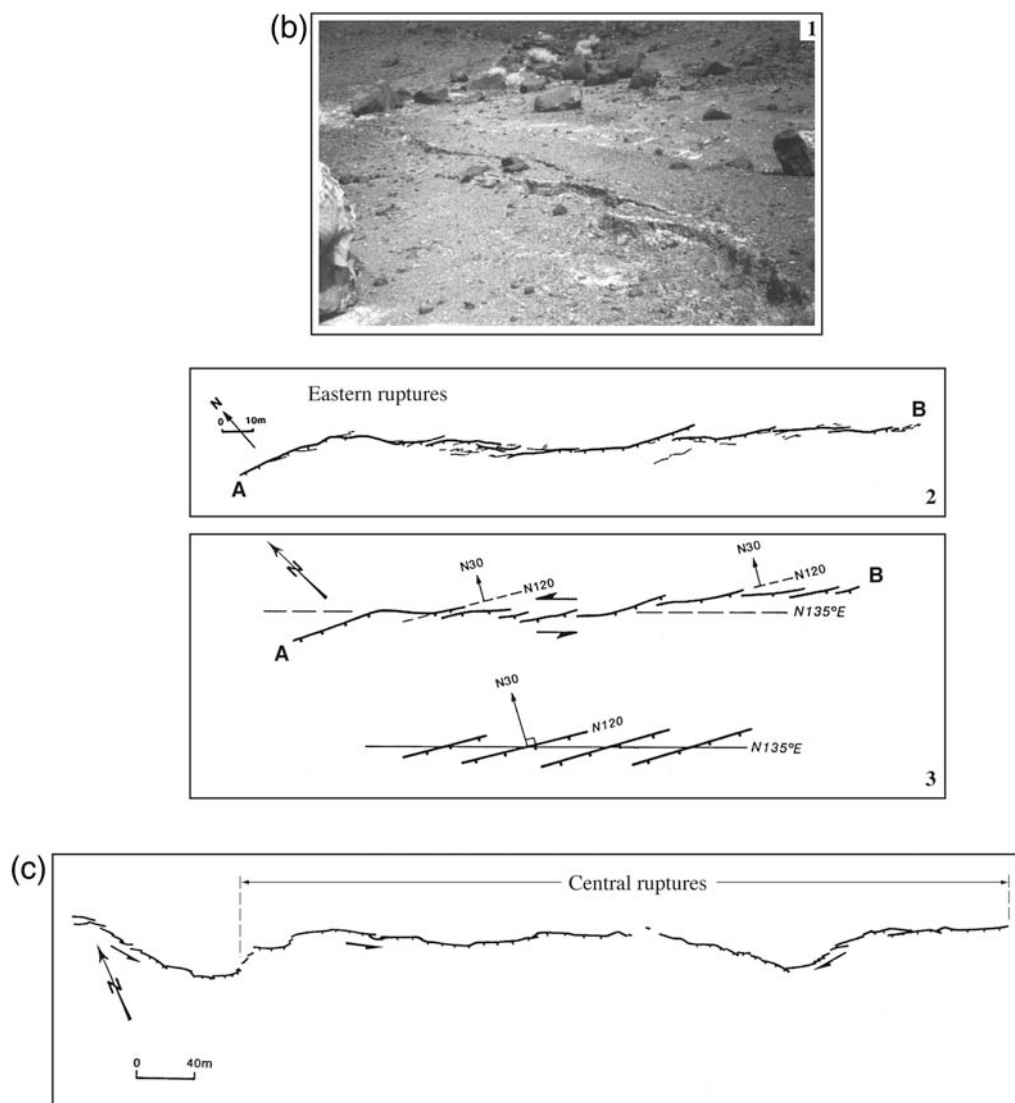


Figure 7. Continued.

be much greater than 60° , because this would result in unstable overhanging ($> 10^\circ$) of the lake beds. Rotating blocks *A* and *C* back to remove the present tilt of block *C* ($16^\circ \pm 1^\circ$) suggests that *F1* may have dipped initially $65\text{--}70^\circ$ SW.

Fissures in area 5 lie ~ 60 m in front of *F1* and ~ 170 m from where block *C* dips under the lake beds (Fig. 8). We infer that *F1* slipped, with the slip refraction right above the volcanic basement-sediment interface. If one adds to the cracks in areas 3 and 5 and the light-colored scarplets along the top of the colluvial wedge between areas 4 and 6, it seems that *F1* must have slipped over a total length of at least 1.6 km during the 1989 sequence, with or without slip-refraction depending on basin depth.

The fissures in areas 1 and 8 are more difficult to explain. In area 1, they lie less than 300 m from the onlapping lake beds upon block *C* and ~ 180 or ~ 300 m away from the base of *F1* and *F2*, respectively. When extrapolated

downward, the flat tilted surface of block *C* suggests that ~ 100 m of sediment overlie the volcanic basement below area 1. A slip mechanism such as depicted in Figure 11 would imply dip values of $\sim 30^\circ$ SW and 20° SW for *F1* or *F2*, respectively (Fig. 12a), 5° to 20° less than those measured at the surface (mean dip of *F1* : $\sim 40^\circ$; mean dip of *F1* fault scarp: $35^\circ\text{--}37^\circ$; comparable to mean dip of *F2* fault scarp on different side views; see Fig. B1 and © Figs. S1 and S3 in the electronic supplement to this paper). Furthermore, seismic slip on *F1* reached the surface in area 6, whereas additional fissures (areas 7 and 8) broke the surface between area 1 and *F2*. We conclude that neither *F1* nor *F2* generated the fissures in area 1.

Trying to explain the fissures in area 8 using the refraction mechanism of Figure 11b and a dip of $\sim 40^\circ$ for *F2* would induce a fissure generation ~ 150 m away from *F2*, while the fissures in area 8 lie less than 60 m from *F2*. Such

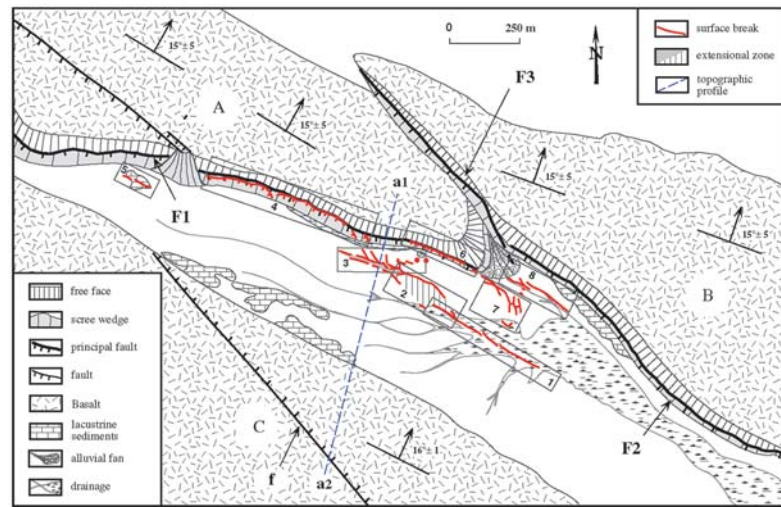


Figure 8. Principal faults and tilted blocks bounding Kadda Hawli half-graben. General map of surface ruptures (outlined in red) measured with total station in February 1993 after 1989 Dôbi earthquake sequence (boxes indicate eight areas mapped in detail).

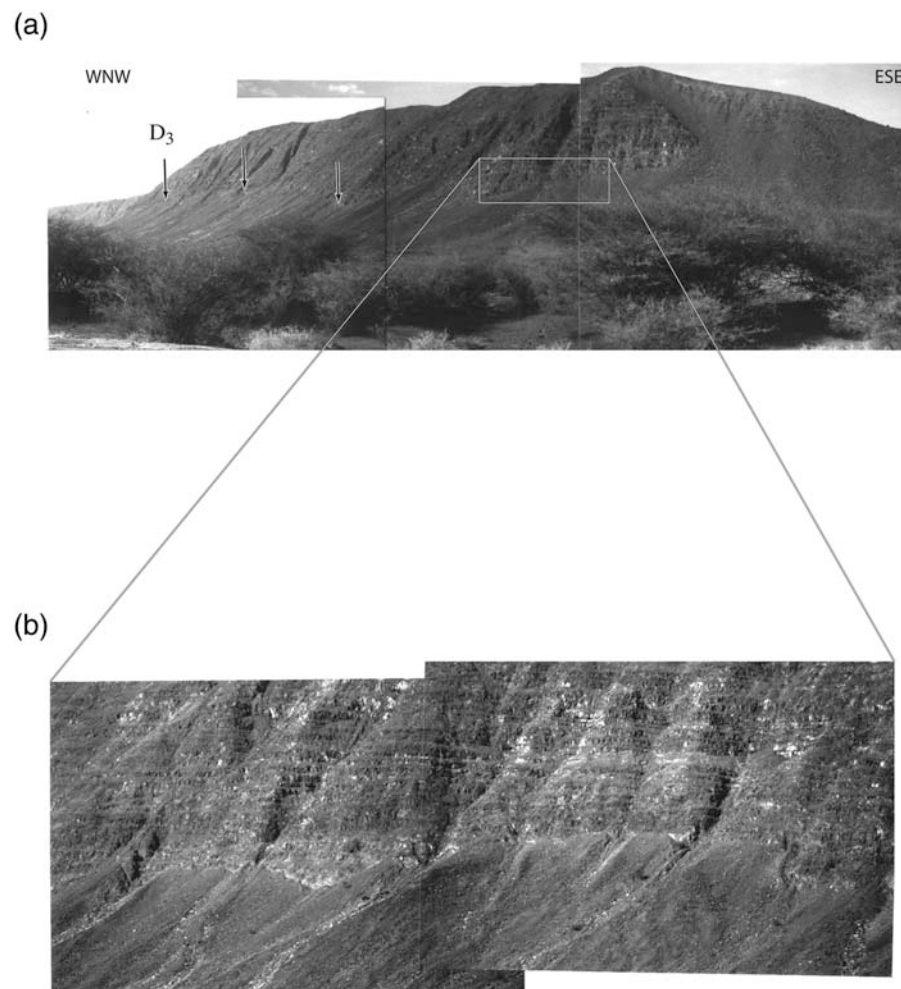


Figure 9. (a) North-looking view of fault-scarp of *D3*. (b) Closeup of light-colored free-faced scarplets along base of *D3* cumulative fault-scarp (c in Fig. 3a).

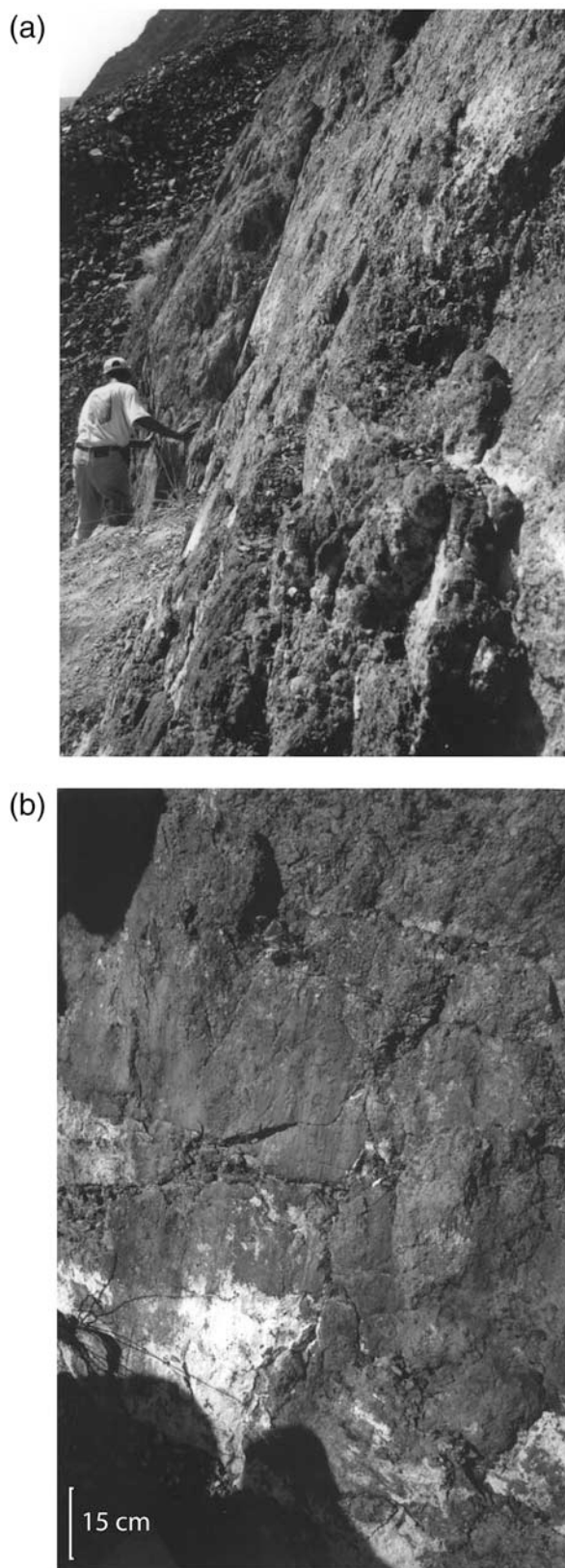


Figure 10. (a) and (b) Photos taken at top of *D3* colluvial wedge at base of free face. (b) View of free-faced scarp base bearing slickensides (pitch of $\sim 80^\circ$ SE). Note lighter color on ~ 30 cm high base of slickensided scarp corresponding to 1989 coseismic exhumation.

a small separation might be taken to imply that *F2* dips 75° SW, but such steepness is implausible given the amount of tilt of the block. One way to reconcile the small separation between the surface cracks and the *F2* scarp with an $\sim 45^\circ$ dip for *F2* would be a thinner sediment layer beneath area 8. That would be the case if another faulted block were hidden by the lake beds between blocks *B* and *C*. If such a block had a surface tilted by $\sim 15^\circ$ northeast (as for *C*) and was bounded on either side by $\sim 50^\circ$ southwest-dipping faults, the place where slip on *F2* would refract into a surface fissure might be below area 8 (Fig. 12b). The location of fault *fe* between this block and *C* would be constrained (as in Fig. 11) by the position of area 1 fissures. The upper tip of this blind block would be ~ 20 m below the half-graben floor (Fig. 12b). Finally, the complex fissures in area 7 (Figs. 8 and B1) might result from faulting of that block by *F3*. Clockwise rotations in the area would be due to dextral shear along *F1*.

The measurements in Kadda Hawli therefore imply, besides *F1* and *F2*, a blind normal fault (*fe*) slipped during the 1989 sequence. These measurements constrain the style of faulting and the superficial stress state. Both *F1* and *F2*, with strikes $\sim N110^\circ E$ and $\sim N125^\circ E$, slipped with a small component of dextral motion. The blind fault *fe*, which generated the $N120^\circ E$ -trending fissures in area 1, also moved with a component of dextral slip. *fe* probably merged with *F1* through areas 2 and 3, forming a dextral, rhomb-shaped connection. The fissures in area 7 were probably caused by clockwise rotation of blocks situated between *fe* and *F1*–*F2*. These fissures may lie directly above the continuation of *F3*, displaced westward by dextral shear on *F1*. Tenuous evidence of left-lateral slip components exists in areas 3, 5, and 8 along surface breaks striking $> N140^\circ E$. Finally, the fissures that strike between $N120^\circ E$ and $N130^\circ E$ show the widest opening. The most likely direction of the maximum extensional stress (σ_3) thus appears to be locally between $N30^\circ$ and $N40^\circ E$, as near Galafi and in ϵ ounda Hawli, but more easterly than in the western part of the Mak ϵ anni depression ($\sim N15^\circ E$; $\text{\textcircled{E}}$ see the electronic supplement to this paper, and Jacques, 1995). The wide scattering of open-fissure strikes ($N80^\circ E$ to $N180^\circ E$) suggests that, near the surface at least, the magnitude of the intermediate stress σ_2 is comparable to that of σ_3 .

Because fissures in area 5 are in the best state of preservation, it is possible to estimate the components of surface seismic slip on them from the total stations measurements. They form a right-lateral \acute{e} chelon along a $N115^\circ E$ direction. The clearest individual fissures have a mean strike of $N130^\circ E$ and are open by ~ 10 cm. Seismic slip on the $N115^\circ E$ -trending fault plane at depth might thus have had right-lateral and extensional components of 3.5 cm and 9.6 cm, respectively. If we assume that the fault plane dips between 45° and 55° , the throw component would have been 10–15 cm, a value similar to the height of the light-colored scarples observed along *F1*.

In summary, our study of the 1989 surface breaks in the region between Galafi and Diciotto to the north shows that more than ten distinct faults were activated by the 1989 D \acute{o} bi

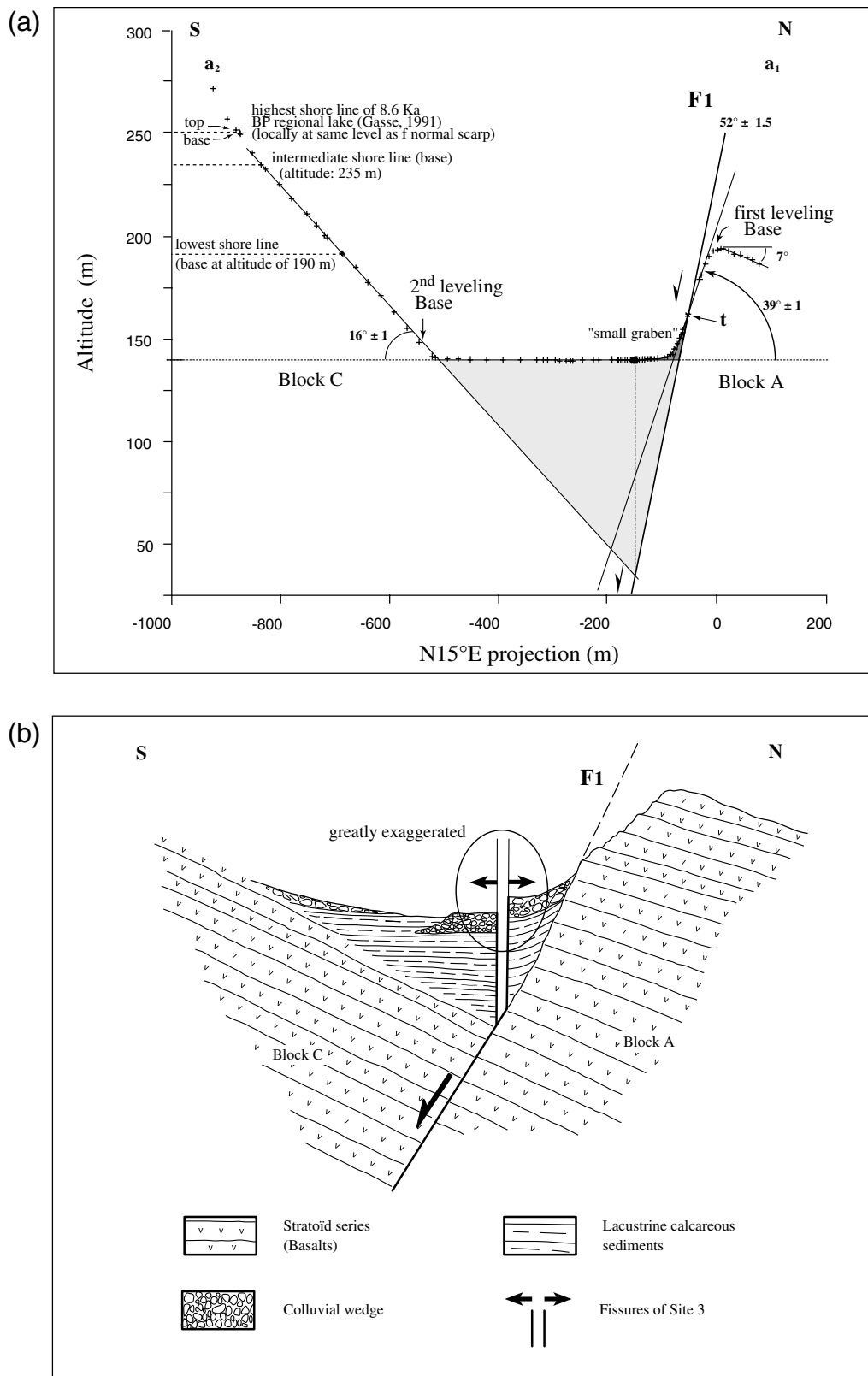


Figure 11. (a) Topographic profile $a_1 - a_2$ (location in Fig. 8) measured with total station across Kadda Hawli half-graben (see Gasse, 1991). Steepest measured dip of $F1$ free face is $39^\circ \pm 1^\circ$. Because of steep slope of $F1$ scarp, only free-face top was leveled from first base. Free-face base (t) is about 7 m above lowest part of profile blind zone. Dip of free surface is thus likely slightly greater than 39° . (b) Schematic interpretation of tectonic and geological section along $a_1 - a_2$.

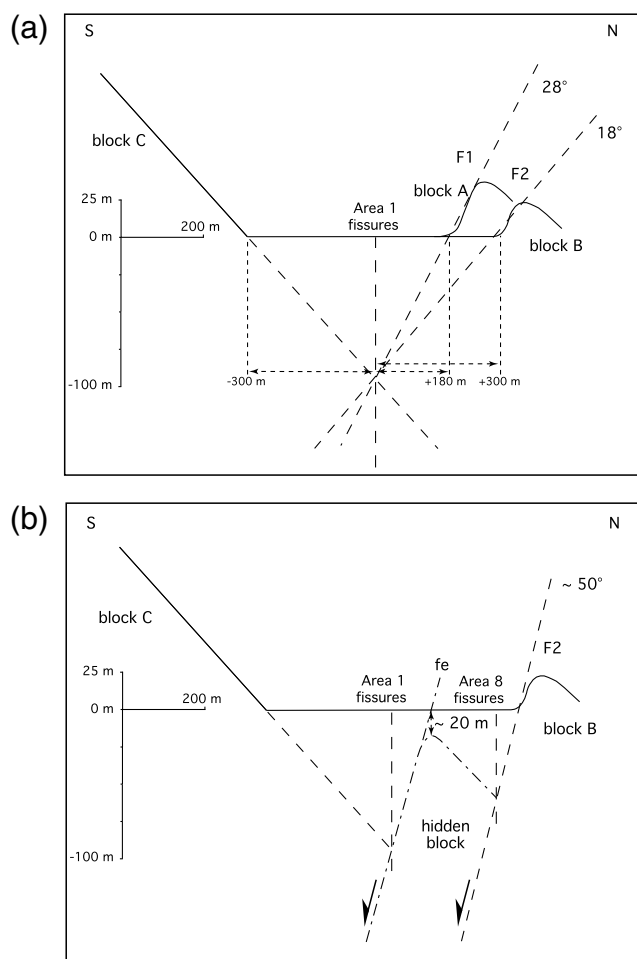


Figure 12. (a) Problem posed by area 1 coseismic fissure location relative to $F1$ and $F2$ cumulative scarps. (b) Preferred interpretative sketch implying small basaltic block hidden beneath sediment infill between blocks B and C (see discussion in text).

earthquakes (Fig. 4b,c). The $N110^\circ \pm 10^\circ E$ -trending faults slipped with a small component of right-lateral motion (10%–30% of the extension), and those striking $\geq \sim N135^\circ E$ with a small left-lateral component (Fig. 5a). The widest fissures imply a minimum principal stress oriented $N30^\circ E$ to $N45^\circ E$ in ϵ ounda Hawli, Kadda Hawli, and near Galafi. Near Mak ϵ anni, σ_3 seems to be oriented $\sim N15^\circ E$ (see the electronic supplement to this paper). The magnitude of the intermediate stress (σ_2) appears to be close to that of σ_3 . The left-lateral slip component and rudder tail termination of $D1$ seem to have induced a local clockwise rotation of σ_3 near Galafi and Kadda Hawli, relative to its regional orientation, as shown in Figure 5b.

The instantaneous faulting kinematics thus appear to be compatible with the longer-term kinematics deduced from a cumulative faulting analysis. Bookshelf faulting about the vertical axes, which is the simplest mechanism to account for strike-slip components of motion along the edges of small parallel blocks, is required to account for the lateral components of brittle faulting in the Galafi–Kadda Hawli region (Fig. 5). The area is located both at the southeast rudder

termination of the normal-sinistral fault $D1$ and between the right-stepping Hanle- ϵ ounda Dôbi and Kadda Dôbi grabens (upper part of Fig. 5c). At the scale of the region in Figure 4b ($20 \times 15 \text{ km}^2$), the $N110^\circ E \pm 10^\circ$ -trending, elongated basaltic slices are thus subject to overall left-lateral shear, which causes them to rotate counterclockwise with right-lateral slip between them. Such rotation and shear are also compatible with left-stepping transfer of left-lateral slip between $D1$ and the Gaggade-Der'êla fault zone (lower part of Fig. 5c).

Probably the most significant effect of this transfer mechanism is to induce an area of counterclockwise rotation, opposite to the rotation (clockwise) documented at the larger scale ($110 \times 130 \text{ km}^2$) throughout central and southern Afar between the Asal–Manda Inakir and Manda Hararo–Goba'ad overlapping rift zones (e.g., Tapponnier *et al.*, 1990; Sigmundsson, 1992; Manighetti, 1993; Manighetti *et al.*, 2001). New paleomagnetic results (Kidane *et al.*, 2003), which indicate that blocks surrounding the Galafi–Kadda Hawli area have not rotated significantly (ϵ ounda Gamarri block, $-2.4^\circ \pm 8.0^\circ$; Galafi–Kadda Hawli area, $-1.3^\circ \pm 7.8^\circ$) or have rotated clockwise (Data-Yager block, $10.0^\circ \pm 8.3^\circ$) are in keeping with this interpretation. In fact, this small region may have suffered an amount of local counterclockwise rotation similar to that of the large-scale, regional clockwise rotation.

Seismotectonics

Although the surface breaks we mapped in the Dôbi Galafi area are small, sparse, and mainly distributed across sedimentary graben floors, there is little doubt that they result from seismic faulting. Most of them are scarplets or fissures zones running along or parallel to the base of cumulative fault scarps. Specifically, the scarplets observed at sites **b** and **c** (Fig. 3a) at Galafi (Fig. 7) and at areas 4, 6, and 8 in Kadda Hawli attest to seismic 1989 slip on $D3$, $D4$, $D5$, $F1$, and $F2$, respectively.

By combining the tectonic study of surface breaks with the relative relocations of the Dôbi earthquakes (Jacques *et al.*, 1999), the focal solutions of the principal shocks, and their source sizes, one can tentatively relate the principal earthquakes of the 1989 sequence to the faults that they ruptured.

Epicentral Locations, Focal Mechanisms, and Source Sizes

The event's epicentral relocations, with assigned errors ranging between $\pm 3 \text{ km}$ and $\pm 10 \text{ km}$ (Table 1; Jacques, 1995; Jacques *et al.*, 1999), were determined using the records of the Djibouti seismological network. Six events ($n=3, 4, 6, 9, 10$, and 11 ; Table 1) could not be located using just the local network, and their epicenters were obtained by adjusting relative relocations from global and local seismological data (Sigmundsson, 1992; Jacques, 1995;

Jacques *et al.*, 1999). The corresponding errors are ± 15 km. Table 1 shows the different estimated magnitudes M_S and m_b published by ISC, while M_L is calculated from local network records (Jacques, 1995). M_w (always larger) is derived from seismic moments published by Braunmiller and Nabelek (1990) and/or Dziewonski *et al.* (1990). For each event, M_L usually ranges between m_b and M_S . As M_L seems more homogenous, it is preferred here to m_b and M_S , and hereafter M refers to M_L .

The source parameters of the principal shocks of the Dôbi sequence (Tables 2 and 3) were obtained from global network data by Dziewonski *et al.* (1990; CMT solutions computed by fixing focal depths at 15 km, except for that of the 20 August 1989 11h16 event, which was calculated to be 16 ± 0.8) and by Braunmiller and Nabelek (1990, from body-waveform inversion). The fault-plane solutions (Fig. 13a) found by Dziewonski *et al.* (1990) and Braunmiller and Nabelek (1990) are in fair agreement, with nodal-plane strikes differing by less than 15° – 20° and dips by less than 5° – 10° (Table 2 and Fig. 13a). The earthquakes were predominantly normal-faulting events (Sigmundsson, 1992), with nodal-planes strikes between $N90^\circ E$ and $N130^\circ E$ (CMT solutions) and between $N100^\circ E$ and $N120^\circ E$ (body-waveform inversions), comparable to those of the main Dôbi graben normal faults. Horizontal projections of slip vectors strike between $N10^\circ E$ and $N30^\circ E$. Specifically, the event at 11h16 on 20 August (M_S 6.2), located in the Galafi–Kadda Hawli region, has a slip-vector striking $\sim N30^\circ E$ on the northeast dipping plane. The fault-plane solutions are compatible with σ_3 oriented $N10^\circ E$ to $N30^\circ E$ in the northern part of the graben and $N30^\circ E$ – $N45^\circ E$ in its eastern part. Oblique lateral components are very small. The nodal-plane dips range from

30° to 60° with maximum values of 45° – 60° . Such dips are smaller than those usually observed in the field (70° – 80°), suggesting that fault dips decrease from surface to depth. Note, however, that in the Galafi–Kadda Hawli region, second-order faults do have surface-dip values ranging between 40° and 60° due to block tilting. Both source parameter determination methods yield the largest seismic moments for the earthquakes that occurred at 11h16 on 20 August and at 1h09 the following day (numbers 1 and 13, Table 1). Dziewonski's *et al.* (1990) moments are slightly larger. The cumulative seismic moment of these two events is $\sim 2/3$ of the total computed moment release of the sequence.

The earthquake source sizes are derived from their seismic moments (M_0) using scaling laws (Kanamori, 1977). Four of the nine M_w derived from the M_0 of Braunmiller and Nabelek (1990) and Dziewonski *et al.* (1990) are greater than M (≥ 0.4), while M is always close to M_S (events at 11h16, 19h25 on 20 August and at 5h03 on 21 August) or m_b (event at 5h05 on 21 August). Thus, we divided the corresponding M_0 by 2, assuming that they were likely determined within a factor 2. The seismic moments not determined by Braunmiller and Nabelek (1990) nor by Dziewonski *et al.* (1990), were derived from M . For dislocation sizes smaller than the effective seismogenic thickness H_{es} ($H_{es} = H_s / \sin \alpha$, where $H_s \sim 13$ km is the local seismogenic thickness and α the fault dip), we use a circular rupture model, assuming a mean stress drop of ~ 30 bars. The circular ruptures are then approximated by square-shaped surfaces having equivalent areas. When the width of the dislocation is $\geq H_{es}$ (e.g., for an $M \geq 6.2$ event on a $\sim 55^\circ$ – 60° dipping fault), we use a scaling law similar to that of Scholz (1990; Jacques, 1995). For even greater ruptures, fault widths,

Table 1
Data for the Principal Earthquakes of the Dôbi Sequence

Event Number	Date (dd)*	Time†	X‡ (km)	Y‡ (km)	Error Location (Horizontal Plane)	Body Wave Magnitude	M_S	M_L	M_w
1	20	11h16	156.7	1302.1	3	5.8	6.2	6.1	6.5
2		11h17	149.3	1305.1	5	5.7	6.5	6.0	6.2
3		11h46	141.7	1313.9	15	6.0	5.8	6.0	6.1
4		11h56	154.9	1307.0	15	5.2	5.9	5.7	–
5		13h25	146.6	1307.3	5	5.2	5.9	5.6	–
6		13h26	142.3	1314.3	15	5.3	6.1	6.1	–
7		14h15	145.2	1307.3	10	4.5	–	5.1	–
8		15h55	150.3	1301.6	5	4.3	–	5.0	–
9		18h27	132.3	1303.9	15	5.1	–	5.3	–
10		18h39	143.7	1312.9	15	5.4	–	5.5	5.7
11		18h54	128.8	1314.9	15	5.3	–	5.3	–
12		19h25	139.4	1317.6	3	6.1	5.8	5.9	6.3
13	21	01h09	147.3	1316.4	3	6.2	6.3	6.3	6.4
14		01h33	150.2	1316.3	5	4.9	–	5.3	–
15		05h03	126.2	1320.8	5	5.7	5.7	5.7	6.3
16		05h05	134.6	1315.9	3	5.2	–	5.2	5.8
17		07h07	135.1	1318.3	10	5.1	4.6	5.2	5.2
18	22	03h01	108.2	1323.3	5	4.7	5.0	5.1	–

*August 1989

†UTC

‡UTM 38 system

Table 2
Fault-Plane Solution Parameters Obtained by [Dziewonski et al. \(1990\)](#)
and [Braunmiller and Nabelek \(1990\)](#)

Day (dd)	Time	Plane 1		Plane 2		M_0 (10^{18} Nm)	Plane 1			M_0 (10^{18} Nm)
		Strike	NW Dip	Strike	SE Dip		Strike	NW Dip	Rake	
20	11h16	301°	45°	121°	45°	6,2	302°	46°	-76°	5,3
	11h17	-	-	-	-	-	298°	31°	-73°	2,3
	11h46	288°	38°	130°	55°	1,6	-	-	-	-
	18h39	294°	45°	114°	45°	0,39	-	-	-	-
	19h25	285°	34°	108°	56°	1,6	295°	29°	-83°	1,8
21	01h09	281°	45°	116°	46°	5,3	292°	42°	-95°	4,4
	05h03	290°	41°	92°	51°	1,6	288°	36°	-87°	1,4
	05h05	296°	45°	116°	45°	0,58	-	-	-	-
	07h07	296°	32°	102°	59°	0,11	-	-	-	-

plausible bounds of fault length deduced from scaling, and length of faults measured on maps are specified.

Earthquakes and Related Faults

It is not straightforward to relate the principal shocks of the Dôbi sequence to the faults they ruptured and to the corresponding observed surface breaks. This is because many faults slipped, and surface signs of seismic ruptures were usually subtle. Besides, the northwestern part of the graben was always too wet or flooded, which hampered fieldwork. We first focused on the largest faults whose slip likely caused the most important and best-located events (Fig. 13b). The smaller and/or less accurately located shocks were subsequently examined. A spatio-temporal scenario of the evolution of the Dôbi earthquake sequence was thus obtained. Although non unique, this scenario accounts best for the combined set of seismic and tectonic observations. The principal shocks are separated in two groups in the southeast and northwest parts of the graben.

Earthquakes in the Southeast Dôbi Graben. Within ± 3 km, the epicenter of the large shock at 11h16 on 20 August (number 1, $M \sim 6.1$ and $M_w \sim 6.5$) falls about 10 km away from the surface traces of two of the largest faults of the southeastern part of the Dôbi graben: *D1a* and *K1a* (Figs. 3a and 13b). The nodal planes of this event dip $\sim 45^\circ$ (Table 2). The northeast-dipping plane P1 strikes $\sim N120^\circ E$ (Fig. 13a; [Dziewonski et al., 1990](#); [Braunmiller and Nabelek, 1990](#)), the southwest-dipping plane P2, $\sim N120^\circ E$ ([Dziewonski et al., 1990](#)) or $\sim N100^\circ E$ ([Braunmiller and Nabelek, 1990](#)). This shock might thus have plausibly ruptured either *K1a* or *D1a*. It should have nucleated at a depth greater than 10 km given the steeper, 70° surface fault dip. The base of the seismogenic crust being at a depth of about 13 km ([Jacques, 1995](#); [Jacques et al., 1999](#)), it is likely that it nucleated at that depth (Fig. 14a).

The strike difference between P1 and the superficial trace of *D1a* is between 5° and 15° ($10^\circ \pm 5^\circ$), while the strike difference between P2 and *K1a* is larger (15° to 35°

or $25^\circ \pm 10^\circ$). This suggests slip on *D1a* rather on *K1a*. One might argue that event 1 took place on *K1a* because ruptures in the Kambourta graben are closer to its epicenter, but they lie in the middle of its floor, which is not in keeping with surface ruptures along *K1a*.

Associating event 1 with the deep rupture of *D1* (Fig. 14a) makes it possible to account for several other observations. Southwest of this event's epicenter, surface ruptures were observed in eight different areas, involving seismic faulting on ten south-dipping faults antithetic to *D1* (Fig. 4). This suggests seismic bookshelf faulting in section (Fig. 14a). The northeast tilted, $N110^\circ E \pm 10^\circ$ -trending, basaltic slices that likely abut against *D1a* at depth, would have slipped relative to one another in response to upward propagating rupture on this fault. This would have occurred either coevally or with some delay, producing numerous, complex surface dislocations. This might be the reason why a spectacular rupture was not visible at the base of *D1*'s scarp. Instead, seismic slip was distributed upward on the southwest-dipping faults, vanishing to zero before reaching the surface. The rupture complexity might be related also to the difference ($\sim 10^\circ$) between the $N120^\circ E$ strike of nodal plane P1 and the $N130^\circ E \pm 5^\circ$ average trend of *D1*'s superficial trace as well as its curvature. Dominant dip slip on the $N130^\circ E$ -striking, ~ 10 km-long segment of *D1a* would in fact entail predominant left-lateral slip on its north-striking section.

Another advantage of relating event 1 to *D1a* is to associate one of the two largest shocks of the Dôbi sequence to one of the two major faults (*D1* and *D3*) bounding the

Table 3
Depths and Rupture Durations Determined by
[Braunmiller and Nabelek \(1990\)](#)

Date (dd/mm)	Time	Depth (km)	Duration (s)
20/08	11h16	5	16
	11h17	4	5
	19h25	6	5
21/08	01h09	6	15
	05h03	7	5

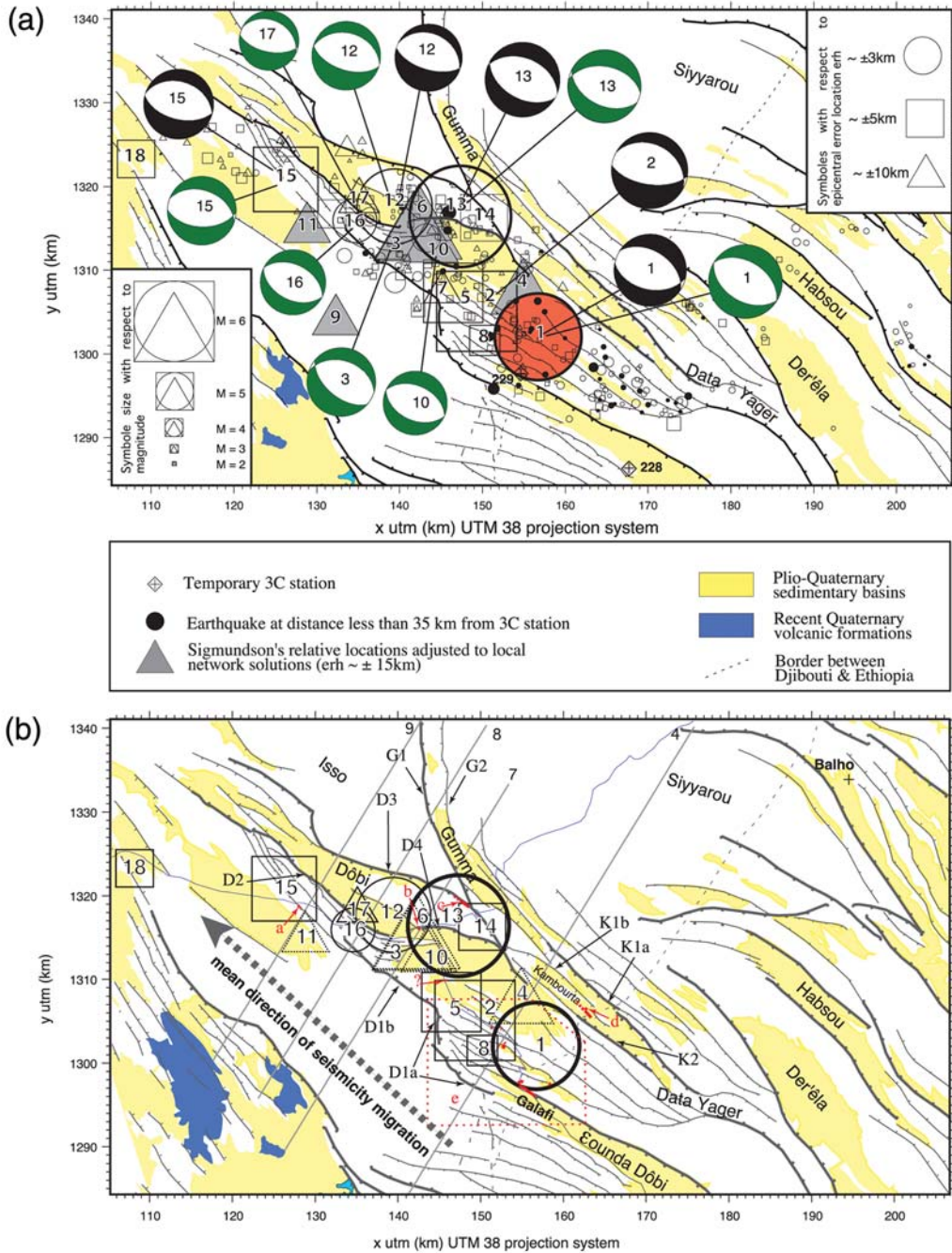


Figure 13. (a) Fault-plane solutions of Dôbi sequence principal shocks. Body-wave modeling solutions of Braunmiller and Nabelek (1990) are drawn in black; CMT solutions of Dziewonski *et al.* (1990) are drawn in dark green. (b) Seismotectonic map of Dôbi region with locations of 1989 $M \geq 5$ earthquakes. Locations of topographic profiles P4, P7, P8, and P9 (drawn in Fig. 14) are shown.

southern and central parts of the graben, where most of the sequence took place (between profiles 2 and 8, Figs. 3a and 13b). Recall that *D1* is the normal fault that has the largest apparent vertical throw (400–450 m downthrow of the Siyyarou relative to the εounda Gamarri block, profiles 4 to 6 in Fig. 3b). A substantial number of small aftershocks and large shocks (event numbers 2, 5, and 8 on 20 August) occurred between the trace of *D1a* and the epicenter of event 1 (Fig. 13b). In Figure 14, the filled small circles re-

present these small aftershocks, the depths of which were accurately determined in this area (Jacques, 1995; Jacques *et al.*, 1999).

In keeping with this interpretation, the seismic moment (M_0) is about 2.9×10^{18} N m, the average fault dip is $\sim 55^\circ$ (Fig. 14a), the fault-width is about 15 km, and the estimated length is between 11 km and 13.5 km. Because the length of *D1a* at the surface is 13 km (Fig. 3a), event 1 probably ruptured all of *D1a* (Fig. 15).

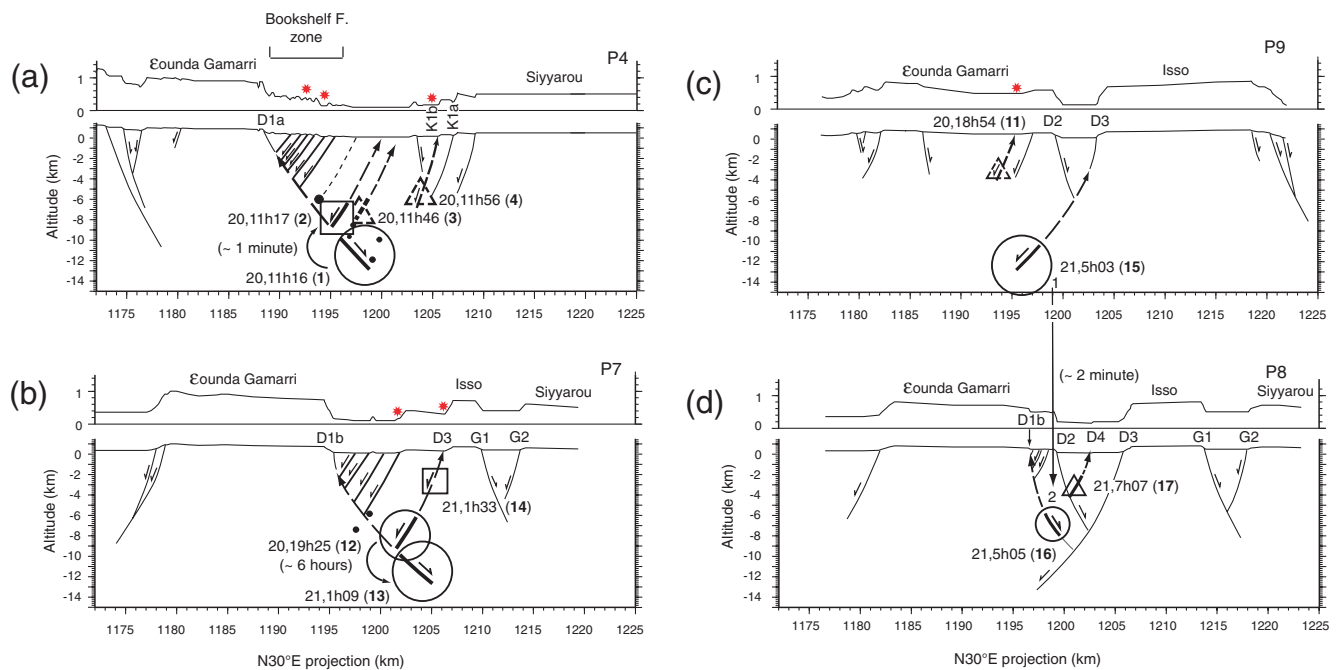


Figure 14. Relationship, in section, between principal shocks and faults activated during Dôbi earthquake sequence (symbols as in Fig. 13). (a) Southeastern part of Dôbi graben (20 August: 11h16, 11h17, 11h46, and 11h56 events). (b) Central part of Dôbi graben (20 August: 19h25 and 21 August: 1h09 and 1h33 events). Northeastern part of Dôbi graben, (c) 20 August: 18h54, 21 August: 5h03 events, and (d) 21 August: 5h05 and 7h07 events. Arrows and durations indicate suggested triggering of shocks separated by short time delay. Stars indicate faults with observed seismic rupture.

The 11h17, 20 August event (number 2, $M \sim 6.0$ and $M_w \sim 6.2$) occurred ~ 50 s after and ~ 8 km northwest of the first mainshock with a location error of ± 5 km (Jacques, 1995; Jacques *et al.*, 1999). Its epicenter lies in the Galafi–Kadda Hawli region (Fig. 13b). The steeper nodal plane of the focal mechanism dips $\sim 60^\circ$ southwest and strikes $\sim N100^\circ E$ (Braunmiller and Nabelek, 1990). The most plausible inference is that this event nucleated at a depth of 8 km on one of the $\sim N115^\circ E$ -trending, 60° southwest-dipping second-order fault abutting *D1a* at depth (Fig. 14a). The seismic moment of this event is about 2.3×10^{18} N m (Braunmiller and Nabelek, 1990), the average fault dip is 65° (Fig. 14a), and the corresponding fault-width is 13 km, although from Figure 14a, it must be ≤ 9 km. The estimated length of the ruptured area ranges between 12 km and 15 km. In Figure 15, the rupture length taken is ~ 13 km.

Surface breaks related to event 2 located in the area of the Dôbi graben would have been liable to flooding at some distance from the road linking the Ethiopian Assab-Addis highway to Djibouti, perhaps not far from the northern border of the graben (*D3* and *D4*). This may be the reason why we could not document such breaks while people living there reported the opening of fissures.

The two events at 13h25 and 15h55 on 20 August (numbers 5 and 8, $M \sim 5.6$ and $M \sim 5.0$, respectively) occurred 2h09 min and 4h39 min after the 11h16 event. Within ± 5 km, they were relocated in the area between the epicenter of event 1 and *D1a*'s fault scarp (Fig. 13b). They probably ruptured

second-order faults bounding the $N110^\circ E \pm 10^\circ$ -trending basaltic slices, causing some of the bookshelf-faulting ruptures observed along these faults. The corresponding seismic moments are 2.8×10^{17} N m and 3.5×10^{16} N m, respectively. The ruptured fault areas activated by these shocks may be approximated by two squares of 6 and 3 km on a side, respectively (Fig. 15).

The epicenter of the event at 14h15 on 20 August (number 7, $M \sim 5.1$) was relocated using the Djibouti network within ± 10 km. It lies a few kilometers northeast of the kink of *D1*. It may have ruptured one of the second-order, antithetic faults abutting *D1* at depth. The moment M_0 of this event is 5.0×10^{16} N m. In Figure 15, its source is represented by a square rupture patch 3.5 km on a side.

The location of the event at 11h56 on 20 August (number 4, $M \sim 5.7$, Fig. 13b), 40 min after the first shock, was obtained by adjusting Sigmundsson's relocation to local ones. Although the uncertainty on this location is ~ 15 km (Jacques, 1995; Jacques *et al.* 1999), this earthquake could have taken place on *K1b* (Fig. 13b) and produced the surface breaks observed in the Kambourta graben (**d** in Fig. 3b). Because these breaks consist of open fissures lying southeast of, but not far off this fault, they might result from a slip-refraction process similar to that observed at Kadda Hawli. The moment M_0 , derived from M is 3.9×10^{17} N m. The fault patch ruptured may be approximated by a square-shaped area of ~ 7 km on a side (Fig. 15).

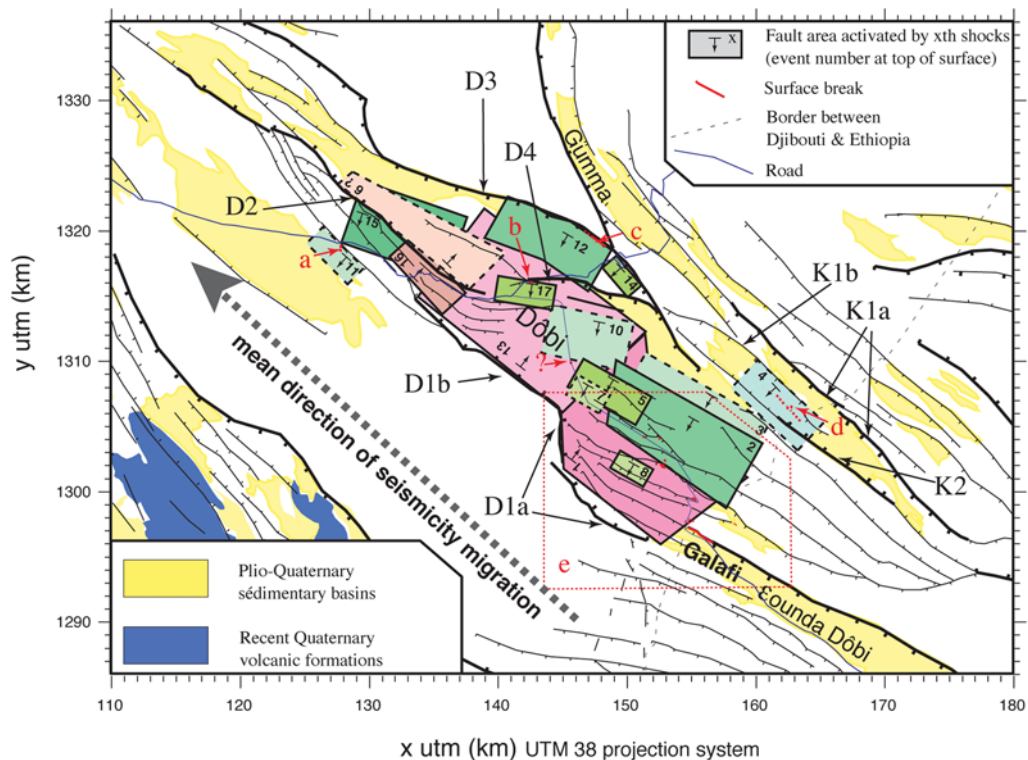


Figure 15. Sketch-map of faults activated by Dôbi sequence earthquakes (event numbers as in Table 1). Ruptured fault patches are projected onto the surface. Patches bordered by dashed lines are poorly constrained. Green and blue patches dip southwest; pink and red patches dip northeast.

Earthquakes in the Central and Northwest Dôbi Graben. The event at 1h09 on 21 August (number 13, $M \sim 6.3$ and $M_w \sim 6.4$) is the largest earthquake of the sequence. As for event 1, the nodal planes dip $\sim 45^\circ$ (Dziwonski *et al.*, 1990; Braunmiller and Nabelek, 1990; Table 2). Braunmiller and Nabelek's (1990) determination yields a steeper dip ($\sim 50^\circ$) for the southwest dipping plane (Fig. 13a). The strike of the northeast dipping nodal plane P1 is $\sim N100^\circ E$ (Dziwonski *et al.*, 1990) or $N110^\circ E$ (Braunmiller and Nabelek, 1990). The southwest-dipping nodal plane P2 strikes $\sim N115^\circ E$ (Dziwonski *et al.*, 1990) or $\sim N120^\circ E$ (Braunmiller and Nabelek, 1990). The epicenter of event 13 is located only 2–3 km southwestward of D3 with an error of ± 3 km (Fig. 13b). It is thus implausible that this large earthquake ruptured D3 because, given its fault dip, it would then have nucleated at only ~ 2 km depth (Fig. 14b). Rather, like event 1, this shock should have nucleated ~ 13 km deep, near the base of the seismogenic layer. Given the 45° dip of the northeast-dipping nodal-plane, the epicenter location would then be consistent with slip on the $N125^\circ E$ -striking, northeast-dipping section D1b of D1 (Fig. 14b). It is quite unlikely that this shock might have ruptured G2 (or the $N140^\circ E$ -striking, northwestern part of K1a) because there was no evidence for recent seismic faulting along the Gumma graben. Furthermore, the minimum strike difference between both of these faults and P2 (20° – 25°) is greater than between D1b and P1 (15°).

We conclude that event 13 nucleated on the deepest part of D1b. As rupture propagated upward, it might have caused distributed slip on second-order antithetic faults abutting D1b above D3, as was the case for event 1. The seismic sources of events 1 and 13 might thus have been similarly complex. In Figure 14b, the mean dip of D1b is $\sim 45^\circ$ at 12 km depth, $\sim 55^\circ$ between 12-km and 6-km depths, and $\sim 70^\circ$ at the surface. M_0 is about 4.9×10^{18} N m (Dziwonski *et al.*, 1990; Braunmiller and Nabelek, 1990), and the fault width is ~ 15 km. The estimated length of the ruptured area ranges from 14 km to 17 km, while the length of D1b measured at the surface in Figure 13 is about 15 km. Therefore, event 13 probably ruptured all of D1b (Fig. 15).

The event at 19h25 on 20 August (number 12, $M 5.8$, $M_w \sim 6.3$) was located 5 km southeast of D3 (Fig. 13b), with an epicentral location error of ± 3 km. The southwest-dipping nodal plane is steeper (56° and 60° , Table 2, Fig. 13a) than the northeast dipping one (34° and 29° , Table 2). Given its location relative to D3, the simplest hypothesis is thus that this shock nucleated near the base of D3 at a depth of 9 km (Fig. 14b). D3 would have an average dip of about 65° ($\sim 60^\circ$ at 6 km depth and $\sim 70^\circ$ at the surface). The moment M_0 chosen for estimating the ruptured fault length is about 8.5×10^{17} N m. The corresponding fault patch that slipped during the earthquake may be approximated by a square-shaped area of ~ 9 km on a side (Fig. 15).

The event at 1h33 on 21 August (number 14, $M \sim 5$) is located south of $D3$ and very close to its trace (Fig. 13b). Given its location error (± 5 km), this event can only be associated with the rupture of the southeast shallowest part of $D3$ (Fig. 15). The event seismic moment is 3.5×10^{16} N m. The slip patch on $D3$ may be approximated by a 3-km square area.

The epicenter of the 5h03 event on 21 August (number 15, $M \sim 5.7$ and $M_w \sim 6.3$) is located about 3 km southwest of the trace of northeast-dipping $D2$ and 8–9 km southwest of $D3$ (Fig. 13b) with a location error of ± 5 km. In the northern part of the graben (between P7 and P10, Fig. 3), the main cumulative fault scarp is that of $D3$ (see P8 and P9 in Fig. 14c,d), and $D2$ probably abuts $D3$ at depth because the ϵ ounda Gamarri block is downthrown ~ 150 m with respect to the Isso block. Given the $\sim N095^\circ E$ strike of its southwest-dipping nodal plane P2 (Dziewonski *et al.*, 1990; Braunmiller and Nabelek, 1990), event 15 thus likely ruptured the northwest part of the latter fault. It might have nucleated at a depth of 10–12 km on $D3$ (as did events 1 and 13 on $D1a$ and $D1b$, respectively; Fig. 14c). This is in keeping with the epicentral location error, and the dip ($\sim 50^\circ$) of the nodal plane P2 (Fig. 13a). The M_0 chosen to estimate the ruptured length is $\sim 7.5 \times 10^{17}$ N m. The surface that slipped may be approximated by a square-shaped area of ~ 8.5 km on a side (Fig. 15).

Together, events 12, 14, and 15 thus seem to have ruptured most of the southeast segment of $D3$, east of its north-directed kink (east of P10, Fig. 13b). One of these events, most likely 12, must have produced the surface rupture observed at site **c** (Figs. 13b, 9, and 10).

The epicentral location of the smaller, and probably shallower, event at 5h05 on 21 August (number 16, $M \sim 5.2$ and $M_w \sim 5.8$) lies in the overlap zone between $D2$ and $D1b$ (Fig. 13). With an uncertainty of ± 3 km, it is located about 3 km east of the northwest termination of $D1b$. It may thus be associated with rupture of the termination of this fault. If so, it would have nucleated at a depth of 7 km (Fig. 14d), and the corresponding source would be an ~ 6 km long square-shaped patch ($M_0 \sim 7.5 \times 10^{17}$ N m; Fig. 15). It might not have caused any surface break.

The epicentral location error for the earthquake at 7h07 on 21 August (number 17, $M_w \sim 5.2$ and $M_w \sim 5.3$) ranges between 5 km and 10 km. Its position relative to $D4$ (Fig. 13b) and its steepest, $N102^\circ E$ -striking, 59° southwest-dipping nodal plane P2 (Dziewonski *et al.*, 1990) suggest that it ruptured the northwestern part of this fault (Fig. 14d). The substantial location error makes it possible that it occurred on one of the small south–southwest dipping faults situated just northwest of the overlapping zone between $D1b$ and $D2$. But the former inference seems more plausible given the surface breaks observed at site **b** (Fig. 15). M_0 being about 1.1×10^{17} N m (Dziewonski *et al.*, 1990), the surface ruptured by this earthquake may be approximated by a square-shaped area of ~ 4.5 km on a side (Fig. 15).

The epicentral locations of the earthquakes at 11h46 (number 3, $M \sim 6.0$ and $M_w \sim 6.1$), 13h26 (number 6,

$M \sim 6.1$), and 18h39 (number 10, $M \sim 5.5$, $M_w \sim 5.7$) on 20 August were obtained by repositioning Sigmundsson's relocations, which were not very accurate (associated errors ~ 15 km) using the epicenters computed from the local network. That all three epicentral positions coincide, in the middle of the Dôbi graben beneath the east–west trending basaltic bridge that connects the opposite graben walls (Fig. 13b) might be taken to imply a computation artifact. The seismic moments M_0 of events 3 and 6 are equal to 1.6×10^{18} N m, that of event 10, to 3.8×10^{17} N m (Dziewonski *et al.*, 1990). The sources of these three events may be approximated by two square-shaped areas 11 km long, and one 6.6 km on a side, respectively (Fig. 15). We suspect that they ruptured southwest-dipping faults between $D1$ – $D2$ and $D3$ – $D4$ (or even parts of $D3$ or $D4$), causing a downthrow of the graben floor, and surface ruptures in or along its boundaries, which were unfortunately flooded most of the time. The fault-plane solutions are compatible with such hypotheses.

Event 3, only 20 min after event 1, may have ruptured a southwest-dipping fault abutting $D1a$ at depth (Fig. 15), as did other shocks in the first hour of the sequence.

Event 6, by contrast, remains one of the major problems of this study. Although it is one of the sequence's principal earthquakes, its location is inaccurate, and its source parameters, including the strike and dip of the fault that slipped, are unknown. Because $D2$ is the only large fault bounding the Dôbi graben to which no other earthquake of the sequence has been associated, however, and because the epicenter of event 6 epicenter lies less than 5 km southeast of $D2$, it might have ruptured this fault (Fig. 14c–d). If this were the case, as $D2$ abuts $D3$ at depth, the ruptured fault width and length might range between 6 and 8 km, and 11.5 and 14.5 km, respectively ($M_0 \sim 1.6 \times 10^{18}$ N m). In the field, we unfortunately failed to see whether the $D2$ fault scarp bore surface rupture traces or not.

The event at 18h54 on 20 August (number 11, $M \sim 5.3$) might have caused the poorly preserved surface ruptures at the base of the fault west of $D2$ near Diciotto (**a** in Figs. 3a and 13b) if it nucleated at a depth shallower than 5 km (Fig. 14c). M_0 (derived from M) being about 10^{17} N m, the surface patch ruptured by this earthquake would be a square-shaped area of ~ 4.5 km on a side (Fig. 15).

The position of the epicenter of the event at 18h27 (number 9, $M \sim 5.3$) on 20 August was obtained by adjusting Sigmundsson's relocations to those computed from the local network. It remains poorly located (Fig. 13a) and falls outside the Dôbi graben ~ 10 km southwestward. Without a fault-plane solution, it is impossible to relate this shock to a fault.

Summary and Discussion

During the 1989 Dôbi earthquake sequence, seismic faulting occurred on at least 15 normal faults cutting the ~ 13 km thick seismogenic crustal layer along the Dôbi

graben. Instead of a single M_w 6.8 event rupturing one of the major faults in a few tens of seconds, a dozen $m_b \geq 5.5$ and $M_S \leq 6.3$ events broke different faults with opposite dip along the edges of, or inside, the graben. That the Afar Serdo sequence of March–April 1969 also involved two main $M > 6$ shocks and seven $M > 5$ events (McKenzie *et al.*, 1970; Gouin, 1979; Kebede *et al.*, 1989) suggests that such a peculiar pattern of elastic strain release is the rule rather than the exception in Afar.

Our study yields a plausible, if not unique scenario of triggered, sequential ruptures on the principal and secondary faults of the Dôbi graben. The two M_S 6.2 and M_S 6.3 mainshocks, ~14 hr apart, seem to have ruptured successively two contiguous sections of the southwest border fault *DI* of the graben. We infer that seismic slip on the two principal bounding faults probably ricocheted from one to the other. The southern, northeast-dipping section *DIa* ruptured first. During this rupture, many shallower, second-order southeast-dipping faults branching off *DI* distributed slip upward, through a vertical bookshelf-faulting mechanism. Later, other secondary faults ruptured, transferring elastic stress and strain from the southern segment of *DI* to *D3*, which dips southwest on the northern side of the graben. This triggered in turn the second mainshock, back on the south side, rupturing the northwestern section *DIb*. Through a domino effect, this faulting mechanism resulted in the rather regular northwestward migration of the principal shocks along the Dôbi graben from *DIa* to *D3* in 18 hr (Jacques *et al.*, 1999; Noir *et al.*, 1997).

Most of the ruptures involved coupled antithetic fault systems, consisting of a deeper main fault and a second-order, shallower fault abutting the former. In such systems, the rupture of one of the two faults is likely to trigger seismic slip on the other straight above or below (Fig. 14). Two mechanisms may account for such interactions. Seismic slip may first occur at depth on the main fault below the intersection zone between the two faults. Deep hanging-wall downthrow then promotes faulting on the second-order fault above by increasing Coulomb stress (mainly by decreasing normal stress) on the latter (Fig. 16a–c). Such a mechanism appears to account for the spatio-temporal relationships between the earthquakes at 11h16, 11h17, and 11h46 on 20 August (Fig. 14a) and between the earthquakes at 5h03 and 5h05 on 21 August (Fig. 14c–d). Alternatively, seismic slip may occur first on the second-order, more superficial fault, with shallow footwall uplift decreasing normal stress and triggering rupture on the main fault below the junction (Fig. 16d). This probably explains the succession of the earthquakes at 19h25 on 20 August and 1h09 the following day (Fig. 14b). Thus, in detail and in 3D, the sequential Dôbi graben faulting, which propagated ~35 km northwestward in ~20 hours, was probably governed by 3D Coulomb stress changes (King *et al.*, 1994; Jacques, 1995), mediated by water flow (Noir *et al.*, 1997), within a crustal volume of ~65,000 km³.

The Dôbi sequence only partly bridges the gap between the largest sequences that occurred in central and eastern

Afar in the last 40 yr, that of Serdo (March–April 1969), and that of Ghoubbet-Asal (November 1978). It leaves the Der'êla half-graben region unruptured. Jacques (1995) pointed out that, on northwest-southeast trending faults in the Der'êla gap region, the Coulomb stress changes caused by the Ghoubbet-Asal sequence, which were already significant (~0.3 bars), increased further after the Dôbi sequence by ~1 bar. Recent tectonic studies have shown that the Der'êla fault system bears clear evidence of Holocene activity (Manighetti, 1993; Manighetti *et al.*, 2001). A critical examination of the historical (Gouin, 1979) and recent seismicity (e.g., Lépine and Hirn, 1992), however, shows no significant earthquake in this region. This suggests that the Der'êla region is ripe for an impending seismic sequence similar to those of Dôbi and Serdo.

The coseismic slip kinematics inferred from the Dôbi sequence are in keeping with those of regional deformation in the last 2 m.y. In the epicentral zone of the first shocks on 20 August, the full vertical throw (600–700 m) of *DI* at depth does not reach the surface. It is absorbed partly by distributed flexural antithetic faulting, with tilting of basaltic blocks bounded by the antithetic faults, through a bookshelf-faulting mechanism in cross section. Likewise, not all the seismic slip of the two largest and deepest shocks of the sequence, which we infer nucleated on the northeast dipping *DI* fault, reached the surface because it was refracted and distributed on these second-order, antithetic faults. Note that block rotation in this process is opposite to that classically involved in hanging-wall rollover, even though *DI* must be listric, with dip decreasing as a function of depth.

A peculiar, small-scale mechanism of rupture refraction at the interface between basement and sediment is observed. It may be of general significance for normal faults bounding basins with poorly consolidated sediment infill. Possible examples may exist in the Abruzzi of central Italy (Avezzano earthquake, e.g., Piccardi *et al.*, 1999; Galadini and Galli, 1999), in the Basin and Range of Nevada (e.g., Caskey *et al.*, 2004), and in Tibet (Armijo *et al.*, 1986; Kapp *et al.*, 2008).

The surface breaks observed in the southeast part of the graben (Galafi–Kadda Hawli region) reveal small components of dextral slip (10%–30% of fault normal extension) along the southwest-dipping, N110°E ± 10°-striking normal faults in the hanging wall of *DI*. A small component of right-lateral slip along the antithetic faults is also manifest in the long-term Quaternary deformation. It may be accounted for by local bookshelf faulting in the horizontal plane, with counterclockwise rotations of ~N110°E-trending basaltic slices about vertical axes. The cause of such rotations is strain transfer between the stepping, northwest-southeast-trending Dôbi and Hanle grabens. Paleomagnetic and tectonic studies (Manighetti *et al.*, 2001; Kidane *et al.*, 2003) show that this counterclockwise rotating subregion lies inside the overlap between the Asal–Manda Inakir and Manda Hararo–Goba'ad rifts, within which northwest-southeast-trending faults, are in turn involved in clockwise bookshelf faulting at a larger regional scale. As a result, finite rotations

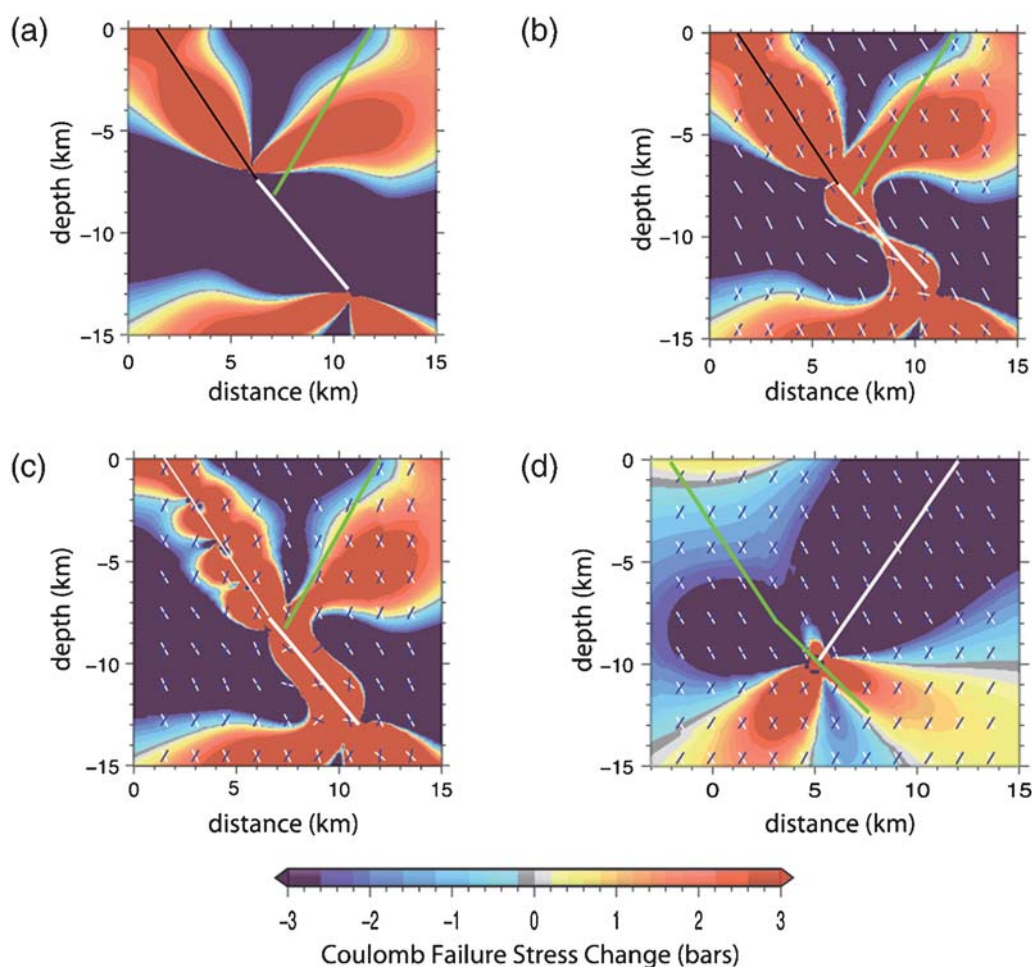


Figure 16. First-order modeling of stress transfer (Coulomb) between two successive events breaking antithetic faults belonging to fault system consisting of deeper, east-dipping main fault, and second-order, shallower, west-dipping fault abutting the former. Figures show Coulomb stress changes in vertical cross section perpendicular to both faults (normal stress and shear stress changes are taken into account, e.g., King *et al.*, 1994; Nostro *et al.*, 2001). Yellow to red colors show Coulomb stress increases, where faulting is promoted; light blue to deep blue colors show Coulomb stress decreases, where faulting is prevented. A horizontal, tensile, deviatoric stress (60 bars) is applied perpendicular to the strike of the faults. Ruptured fault patches are drawn as white segments, and the analyzed fault is drawn as a green line. (a) and (b) Coulomb stress changes caused by rupture on the main east-dipping fault patch (white) computed (a) on west-dipping, normal faults parallel to second-order fault (in green) and (b) on optimally oriented, normal faults (small blue and white segments). (c) Same as (b) except that rupture is distributed along entire main fault plane, with largest slip between 8 and 13 km depth. Rupture of deeper main fault promotes rupture of abutting, antithetic, shallower fault, which lies mostly in areas of high coulomb stress rise (up to several bars) and is oriented nearly parallel to optimally east-dipping normal faults. (d) Coulomb stress changes caused by rupture of second-order fault (white), computed on normal, optimally oriented faults (indicated by small blue and white segments). Note that below intersection between the two faults, the green main fault (between 10 and 13 km depth) is in an area of high Coulomb stress rise ($> \sim 1$ bar). (a), (b), and (c) may explain, for instance, the succession of events at 11h16 and at 11h17 on 20 August 1989, see Figure 14a. (d) may explain, for instance, the succession of events at 19h25 on 20 August (rupture of shallow, second-order fault) and 01h09 on 21 August 1989, which likely nucleated on main fault at a depth of about 12 km, see Figure 14b.

nearly cancel out locally due to two opposite, imbricate bookshelf-faulting mechanisms about vertical axes. This is merely a consequence of the history of strain localization, rather than of changes in large-scale boundary conditions.

Given the unusual density of active faults of different orientations, it is likely that the complexity of the Dôbi sequence, with intricate but well organized fault interactions, typifies that of most multievent sequences in Central Afar, as well as in the Gulf of Tadjourah (1973) and in the southern Red Sea (1967, 1978). It may also be common in other

regions of distributed normal faulting elsewhere in the world, such as Calabria (Jacques *et al.*, 2001), the Abruzzi in Central Italy (Nostro *et al.*, 2005), the Gulf of Corinth in Greece (Hubert *et al.*, 1996), the North Aegean (Nalbant *et al.*, 1998), and the Basin and Range of Nevada (Hodgkinson *et al.*, 1996; Caskey and Wenousky, 1997; Caskey *et al.*, 2004). Such organized fault coupling partly explains the difficulties encountered in interpreting previous Afar seismic sequences from sparser data (e.g., 1969, Gouin [1979]; 1978, Le Dain *et al.* [1979]). Models averaging strain over areas

tens to hundreds of kilometers on a side cannot account for the actual rupture mechanisms of such earthquake sequences. It is thus essential to study faulting at different time and spatial scales in order to understand how the hierarchy of imbricate structures of different sizes and the history of fault growth and propagation govern the finite kinematics of long-term deformation.

Data and Resources

The seismotectonic observations and measurements presented in detail in this paper are original and were collected during several field trips in Djibouti and Ethiopia. The seismological data used in this paper come from published sources listed in the references.

Acknowledgments

We thank the Centre d'études et de recherche de Djibouti (CERD), particularly its two successive directors, J. Mohamed and A. Abdallah (when CERD was Institut Supérieur d'Etudes et de Recherches Scientifiques et Techniques), and the Earth Science department of Addis Ababa University for their scientific collaboration and logistic support. We are grateful to four anonymous reviewers for their constructive comments. This work was supported by Institut National des Sciences de l'Univers (INSU, Paris, France; Dynamique Bilan Terre scientific program). The Système Probatoire d'Observation de la Terre satellite imagery was acquired through the TECTOSCOPE program (IST scientific program, INSU) cosponsored by the Centre National d'Etudes Spatiales (CNES, France). This contribution is Institut de Physique du Globe de Paris no. 3113. This contribution is Institut de Physique du Globe de Strasbourg. This contribution is Earth Observatory of Singapore no. 19.

References

- Abdallah, A., V. Courtillot, M. Kasser, A. Y. Le Dain, J. C. Lépine, B. Robineau, J. C. Ruegg, P. Tapponnier, and A. Tarantola (1979). Afar seismicity and volcanism: Relevance to the mechanics of accreting plate boundaries, *Nature* **282**, 17–23.
- Acton, G. D., S. Stein, and J. F. Engeln (1991). Block rotation and continental extension in Afar: A comparison to oceanic microplate system, *Tectonics* **10**, 501–526.
- Armijo, R., P. Tapponnier, J. L. Mercier, and H. Tong-Lin (1986). Quaternary extension in southern Tibet: Field observations and tectonic implications, *J. Geophys. Res.* **91**, no. B14, 13803–13872.
- Ayele, A., E. Jacques, M. Kassim, T. Kidane, A. Omar, S. Tait, A. Nercessian, J. B. de Chabaliér, and G. King (2007). The volcano-seismic crisis in Afar, Ethiopia, starting September 2005, *Earth Planet. Sci. Lett.* **255**, 177–187.
- Ayele, A., D. Keir, C. Ebinger, T. Wright, G. Stuart, B. Buck, E. Jacques, Gh. Ogubazghi, and J. Sholan (2009). September 2005 mega-dike emplacement in the Manda Hararo nascent oceanic rift (Afar depression), *Geophys. Res. Lett.* **36**, L20306, doi [10.1029/2009GL039605](https://doi.org/10.1029/2009GL039605).
- Braunmiller, J., and J. Nabelek (1990). The 1989 Ethiopia earthquake sequence, *Eos Trans. AGU* **71**, 1480.
- Caskey, S. J., and S. W. Wenousky (1997). Static stress changes and earthquake triggering during the 1954 Fairview Peak and Dixie Valley earthquake, Central Nevada, *Bull. Seismol. Soc. Am.* **87**, 521–527.
- Caskey, S. J., J. W. Bell, A. R. Ramelli, and S. W. Wenousky (2004). Historic surface faulting and Paleoseismicity in the area of the 1954 Rainbow Mountain-Stillwater earthquake sequence, central Nevada, *Bull. Seismol. Soc. Am.* **94**, 1255–1275.
- Consiglio Nazionale delle Ricerche and Centre National de la Recherche Scientifique (1975). Geological Map of Afar, 2, Central and Southern Afar, Geotechnip, La Celle St. Cloud, France, scale: 1/500000.
- Courtillot, V., J. Achache, F. Landre, N. Bonhommet, R. Montigny, and G. Féraud (1984). Episodic spreading and rift propagation: New paleomagnetic and geochronologic data from the Afar nascent passive margin, *J. Geophys. Res.* **89**, no. B5, 3315–3333, doi [10.1029/JB089iB05p03315](https://doi.org/10.1029/JB089iB05p03315).
- Daëron, M., Y. Klinger, P. Tapponnier, A. Elias, E. Jacques, and A. Surssock (2005). Sources of the large A.D. 1202 and 1759 Near East earthquakes, *Geology* **33**, 529–532.
- Dziewonski, A. M., G. Ekström, J. H. Woodhouse, and G. Zwart (1990). Centroid-moment tensor solutions for July–September 1989, *Phys. Earth Planet. In.* **62**, 185–193.
- Ebinger, C. J., D. Keir, A. Ayele, E. Calais, T. Wright, M. Belachew, J. Hammond, M. Campbell, and R. Buck (2008). Capturing magma intrusion and faulting process during continental rupture: Seismicity of the Dabbahu (Afar) rift, *Geophys. J. Int.* **174**, 1138–1152.
- Ethiopian Mapping Agency (EMA) (1979). *Urikomam Terara (Ethiopia) & Serdo (Ethiopia) French Territory of Afar and Issas maps (Sheets ND 37-16 & NC 37-4)*, scale 1:250,000, Addis Ababa.
- Galadini, F., and P. Galli (1999). The Holocene paleoearthquakes on the Avezano earthquake faults (central Italy): Implications for active tectonics in the central Apennines, *Tectonophysics* **308**, 143–170.
- Gasse, F. (1991). Tectonic and climatic controls on lake distribution and environments in Afar from Miocene to present, Lacustrine basin exploration: Case studies and modern analogs, B. Katz (Ed.), *AAPG Mem.* **50**, 19–41.
- Gouin, P. (1979). *Earthquake history of Ethiopia and the north of Africa*, Int. Dev. Res. Centre, Edit. 118E, Ottawa, 259 p.
- Grandin, R., A. Socquet, R. Binet, Y. Klinger, E. Jacques, J. B. De Chabaliér, G. King, C. Lasserre, S. Tait, P. Tapponnier, A. Delorme, and P. Pinzuti (2009). September 2005 Manda Hararo–Dabbahu rifting episode, Afar (Ethiopia): Constraints provided by geodetic data, *J. Geophys. Res.* **114**, B08404, doi [10.1029/2008JB005843](https://doi.org/10.1029/2008JB005843).
- Granier, T. (1985). Origin, damping, and pattern of development of faults in granite, *Tectonics* **4**, 721–737.
- Hodgkinson, K. M., R. S. Stein, and G. C. P. King (1996). The 1954 Rainbow Mountain-Fairview Peak-Dixie Valley earthquakes: A triggered normal faulting sequence, *J. Geophys. Res.* **101**, 25459–25471.
- Hubert, A., G. C. P. King, R. Armijo, B. Meyer, and D. Papanastassiou (1996). Fault reactivation, stress interaction and rupture propagation in the 1981 Corinth earthquake sequence, *Earth Planet. Sci. Lett.* **142**, no. 3–4, 573–585.
- Institut Géographique National (IGN) (1953). *Abhe and Gamari Topographic maps*, scale 1:100,000, Paris.
- International Seismological Centre (1991). *Regional Catalogue of Earthquake*, 26 (July–December 1989), Thatcham, 445 p.
- Jacques, E., (1995). *Fonctionnement sismique et couplage élastique des failles en Afar*, *Master's Thesis*, Université Paris, 7-IPGP, December 1995, 485 pp. (in French).
- Jacques, E., C. Monaco, P. Tapponnier, L. Tortorici, and T. Winter (2001). Faulting and earthquake triggering during the 1783 Calabria seismic sequence, *Geophys. J. Int.* **144**, 147, 499–516.
- Jacques, E., J. C. Ruegg, J. C. Lépine, P. Tapponnier, G. C. P. King, and A. Omar (1999). Relocation of $M \geq 2$ events of the 1989 Dôbi seismic sequence in Afar: Evidence for earthquake migration, *Geophys. J. Int.* **138**, 447–469.
- Kanamori, H. (1977). The energy release in great earthquakes, *J. Geophys. Res.* **82**, 2981–2987.
- Kapp, P., M. Taylor, D. Stockli, and L. Ding (2008). Development of active low-angle normal fault system during orogenic collapse: Insight from Tibet, *Geology* **36**, 7–10.
- Kebede, F., W. Kim, and O. Kulhanek (1989). Dynamic source parameters of the March–May 1969 Serdo earthquake sequence in Central Afar,

- Ethiopia, deduced from teleseismic body waves, *J. Geophys. Res.* **94**, 5603–5614.
- Kidane, T., V. Courtillot, I. Manighetti, L. Audin, P. Lahitte, X. Quidleur, P. Y. Gillot, Y. Gallet, J. Carlot, and T. Haile (2003). New paleomagnetic and geochronologic results from Ethiopian Afar, Block rotations linked to rift overlap and propagation and determination of a ~2 Ma reference pole for stable Africa, *J. Geophys. Res.* **108**, no. B2, 2102–2134, doi [10.1029/2001JB000645](https://doi.org/10.1029/2001JB000645).
- King, G., Y. Klinger, D. Bowman, and P. Tapponnier (2005). Slip-partitioned surface breaks for the M_w 7.8 2001 Kokoxili earthquake, China, *Bull. Seismol. Soc. Am.* **95**, 731–738, doi [10.1785/0120040101](https://doi.org/10.1785/0120040101).
- King, G. C. P., R. S. Stein, and J. Lin (1994). Static stress changes and the triggering of earthquakes, *Bull. Seismol. Soc. Am.* **84**, 935–953.
- Klinger, Y., X. Xu, P. Tapponnier, J. Van der Woerd, C. Lasserre, and G. King (2005). High-resolution satellite imagery mapping of the surface rupture and slip distribution of the M_w 7.8, 14 November 2001 Kokoxili earthquake, Kunlun fault, Northern Tibet, China, *Bull. Seismol. Soc. Am.* **95**, 1970–1987, doi [10.1785/0120040233](https://doi.org/10.1785/0120040233).
- Le Dain, A. Y., B. Robineau, and P. Tapponnier (1979). Les effets tectoniques de l'événement sismique et volcanique de novembre 1978 dans le rift d'Asal-Ghoubbet, *Bull. Soc. Geol. Fr.* **22**, 817–822 (in French).
- Lépine, J. C., and A. Hirn (1992). Seismotectonics in the Republic of Djibouti, linking the Afar depression and the Gulf of Aden, *Tectonophysics* **209**, 65–86.
- McKenzie, D. P., D. Davies, and P. Molnar (1970). Plate tectonics of the Red Sea and East Africa, *Nature* **226**, 243–248.
- Manighetti, I. (1993). Dynamique des systèmes extensifs en Afar, *Thèse de Doctorat*, Université Paris, 6 pp. (in French).
- Manighetti, I., P. Tapponnier, P. Y. Gillot, E. Jacques, V. Courtillot, R. Armijo, J. C. Ruegg, and G. C. P. King (1998). Propagation of rifting along the Arabia-Somalia plate boundary: Into Afar, *J. Geophys. Res.* **103**, 4947–4974.
- Manighetti, I., P. Tapponnier, V. Courtillot, Y. Gallet, E. Jacques, and P. Y. Gillot (2001). Strain transfer between disconnected, propagating rifts in Afar, *J. Geophys. Res.* **106**, 13,613–13,665.
- Michetti, A. M., F. Brunamonte, L. Serva, and E. Vittori (1996). Trench investigation of the 1915 Fucino earthquakes, *J. Geophys. Res.* **101**, 5921–5936.
- Muir-Wood, R., and G. C. P. King (1993). Hydrological signatures of earthquake strain, *J. Geophys. Res.* **98**, 22035–22068.
- Nalbant, S., A. Hubert, and G. C. P. King (1998). Stress coupling in north west Turkey and the north Aegean, *J. Geophys. Res.* **103**, 24,469–24,486.
- Noir, J., E. Jacques, S. Békri, P. M. Adler, P. Tapponnier, and G. C. P. King (1997). Fluid flow triggered migration of events in the 1989 Dobi earthquake sequence of Central Afar, *Geophys. Res. Lett.* **24**, 2335–2338.
- Nostro, C., L. Chiaraluce, M. Cocco, D. Baumont, and O. Scotti (2005). Coulomb stress changes by repeated normal faulting earthquakes during the 1997 Umbria–Marche (central Italy) seismic sequence, *J. Geophys. Res.* **110**, B05S20, doi [10.1029/2004JB003386](https://doi.org/10.1029/2004JB003386).
- Nostro, C., A. Piersanti, and M. Cocco (2001). Normal fault interaction caused by coseismic and postseismic stress changes, *J. Geophys. Res.* **106**, 19,391–19,410, doi [10.1029/2001JB000426](https://doi.org/10.1029/2001JB000426).
- Piccardi, L., Y. Gaudemer, P. Tapponnier, and M. Boccaletti (1999). Active oblique extension in the central Apennines (Italy): Evidence from the Fucino basin, *Geophys. J. Int.* **139**, 499–530.
- Scholz, C. H. (1990). *The Mechanics of Earthquakes and Faulting*, Cambridge University Press, Cambridge, 439 pp.
- Sigmundsson, F. (1992). Tectonic implications of the 1989 Afar earthquake sequence, *Geophys. Res. Lett.* **19**, 877–880.
- Rogon, P., and F. Gasse (1972). Néotectonique des dépôts lacustres de l'Holocène inférieur du graben de Dôbi (Afar, Ethiopie), *C. R. somm. Soc. Geol. Fr.* 208–212 (in French).
- Rowland, J., E. Baker, C. Ebinger, D. Keir, T. Kidane, J. Biggs, N. Hayward, and T. J. Wright (2007). Fault growth at a nascent slow-spreading ridge: 2005 Dabbahu rifting episode, Afar, *Geoph. J. Int.* doi [10.1111/j.1365-246X.2007.03584.x](https://doi.org/10.1111/j.1365-246X.2007.03584.x)
- Tapponnier, P., R. Armijo, I. Manighetti, and V. Courtillot (1990). Bookshelf faulting and horizontal block rotation between overlapping rifts in southern Afar, *Geophys. Res. Lett.* **17**, no. 1, 1–4.
- U.S. Geological Survey, (1989). *Earthquake Data Rept.*, 8-89, part 2 of 2, 151–302.
- Varet, J., and F. Gasse (1978). *Geology of central and southern Afar (Ethiopia and Djibouti Republic)*, Centre National de la Recherche Scientifique, Paris.
- Van der Woerd, J., A. Meriaux, Y. Klinger, F. J. Ryerson, Y. Gaudemer, and P. Tapponnier (2002). The 14 November 2001 $M_w = 7.8$ Kokoxili earthquake in Northern Tibet (Qinghai Province, China), *Seismol. Res. Lett.* **73**, 125–135.
- Ward, S., and G. Valensise (1989). Fault parameters and slip distribution of the 1915 Avezano, Italy, earthquake derived from geodetic observations, *Bull. Seismol. Soc. Am.* **79**, 690–710.
- Wright, T. J., C. Ebinger, J. Biggs, A. Ayele, G. Yirgu, D. Keir, and A. Stork (2006). Magma-maintained rift segmentation at continental rupture in the 2005 Afar dyking episode, *Nature* **442**, 291–294.
- Xiaohan, L. (1983). I: Perturbations de contraintes liées aux structures cassantes dans les calcaires fins du Languedoc. Observations et simulations mathématiques. II: Mesure de la déformation finie à l'aide de la méthode FRY. Application aux gneiss de Bormes (Massif des Maures), *Thèse de Doctorat*, Université des Sciences et Techniques du Languedoc (in French).

Appendix A

Overall Damage Reported during the Dôbi Earthquake Sequence

The 1989 Dôbi earthquake sequence caused severe damage to the two checkpoints on either side of the Ethiopia–Djibouti border. The French army-built wall around the Galafi (Djibouti) border checkpoint collapsed, the watchtowers were extensively fissured, and the water tower was ruined. By contrast, the single-story woodframe buildings were little affected. The guards reported that it was difficult to stand at the beginning of the sequence. These effects at the Djiboutian border post, located about 5 km away from the epicenter of the first largest shock (M_S 6.2, 11h16 on 20 August 1989), correspond to an intensity of VIII to IX on the Modified Mercalli (MM) scale. In Yoboki, a village about 40 km southeast of the 11h16 epicenter (Fig. 3a), the walls of certain houses, made of poorly cemented basalt blocks, fell partly. This corresponds to an MM intensity of VI–VII, even though the ultimate damage observed resulted from repeated shaking by several shocks of the sequence. The first mainshock was also felt by most of the inhabitants of Arta (about 110 km away from the epicenter). People working at the Arta Geophysical Observatory observed ripples on the surface of liquids in bottles (MM intensity ~IV–V). After the first shock, the Earth Data Report (numbers 8–89, USGS, 1989) reported two people being killed in the Republic of Djibouti (by rock falls in a wadi near Galafi), and the International Seismological Centre (1991) reported four casualties on the Ethiopian side, extensive destruction at Diciotto (intensity of IX), and the collapse of six bridges (reports from the Addis Ababa Observatory). The second largest shock at 1h09 (M_S 6.3, 21 August 1989) was also felt at Arta, shaking beds in ways similar to those

due to vibrations caused by the passing of a heavy truck (MM intensity \sim IV). The earthquakes with magnitude ≥ 5.5 were felt by some people at rest in Arta and Djibouti (intensity \sim II).

Appendix B

Detailed Geometry of Seismic Surface Breaks in the Galafi–Kadda Hawli Region

The longest and densest arrays of surface breaks were discovered in the Galafi–Kadda Hawli region (box **e** in Fig. 3a). We describe the measurements made along those surface breaks we could reach in 1989, 1993, and 1994. This is also where 15 $M_L \geq 3$ shocks, three of which with magnitudes $5 < M_L \leq 6$ (at 11h56, 13h25, and 14h15 on 20 August, Table 1) and two with magnitudes ≥ 6 (at 11h16 and 11h17 on 20 August) were relocated (Jacques, 1995; Jacques *et al.*, 1999). The M_S 6.2, 11h16 event, in particular, is one of the two largest shocks of the sequence. We mapped the breaks and associated landforms using a digital total-station Wild DI3000-T2000.

The fact that we could not follow surface ruptures for distances greater than ~ 6 km at Galafi, ~ 1.5 km at Kadda Hawli, or several hundred meters elsewhere, with most of the individual breaks or fissures being, at most, a few hundred meters long, may be due to various factors. First, because we were only granted access to Ethiopia four years after the 1989 sequence, stretches of surface ruptures across sedimentary floors may have been obliterated by seasonal floods. Also, we could never examine the westward extension of the Galafi ruptures on the Ethiopian side of the border, because of unrest in this general area. Second, as is clear in Figure 4, the zones floored with lacustrine sediments, where surface ruptures are easily identified, cover less than half of the total surface of the Galafi–Kadda Hawli region. The rest is covered with stratoid basalts forming boulder fields. Because vertical throws of the seismic surface ruptures are usually less than 30 cm, on order of boulder size, fissures cutting basalt surfaces are easily missed.

Surface Breaks near Galafi

Near Galafi, the longest rupture zone found lies along the base of the $D5$ scarp (Figs. 4b and 7). It can be followed southeastward of the Djibouti–Ethiopia border for ~ 6 km. About 600 m and 1000 m north-northwest of the check post, two similar alignments of surface breaks were observed, also along the base of two northeastward tilted blocks (Fig. 7a). We mapped the former rupture, which strikes $N75^\circ E$ to $N135^\circ E$ for about 1 km. The vertical throw and width are maximum along $N120^\circ E$ -trending sections, reaching highs and widths of up to 30 cm and 15 cm, respectively (Manighetti, 1993). $N135^\circ E$ -trending fault segments have a left-lateral slip component (Fig. 7b), $N65^\circ E$ - to $N115^\circ E$ -striking segments, and a right-lateral slip component (Fig. 7c). This is consistent with σ_3 being locally oriented at $N30^\circ E$.

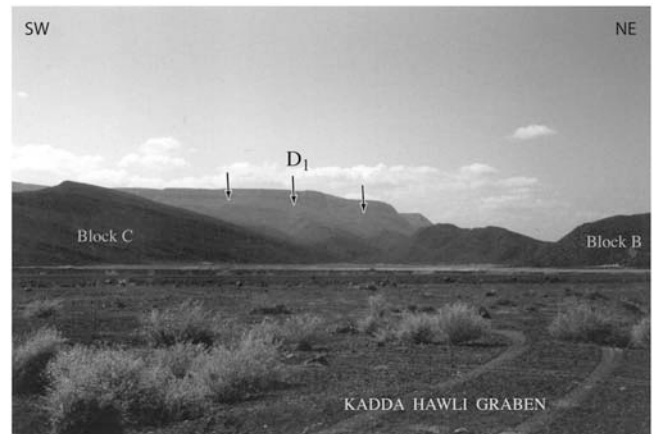


Figure B1. Northwest-looking view of Kadda Hawli half-graben. Floor is 139 m above sea level. Note tilted block *C* dipping 15° – 20° northeast and 35° – 40° southwest-dipping cumulative escarpments, as well as kink of $D1$ in background.

From detailed measurements of $N120^\circ E$ -striking individual breaks, the slip-vector on one $N135^\circ E$ -trending segment appears to have the following components: $x = 3.9$ cm (left-lateral, parallel to $N135^\circ E$), $y = 14.5$ cm (perpendicular to $N135^\circ E$), and $z = 30$ cm (vertical). On a $N115^\circ E$ -trending fault, parallel to the average strike of $D5$ near Galafi, the horizontal components of the slip vector would thus be $x = 1.3$ cm (right-lateral, parallel to $N115^\circ E$) and $y = 14.9$ cm (perpendicular to $N115^\circ E$). Hence, $D5$ probably moved during the earthquake sequence with a small oblique, right-lateral component of slip, of about one tenth of the extensional slip.

Surface Breaks in the Kadda Hawli Half-Graben

The Kadda Hawli trough (Fig. B1) is partly filled with lacustrine sediments. It lies on the hanging wall of the southern termination of $D1$, ~ 8 km east of the kink of $D1$ and

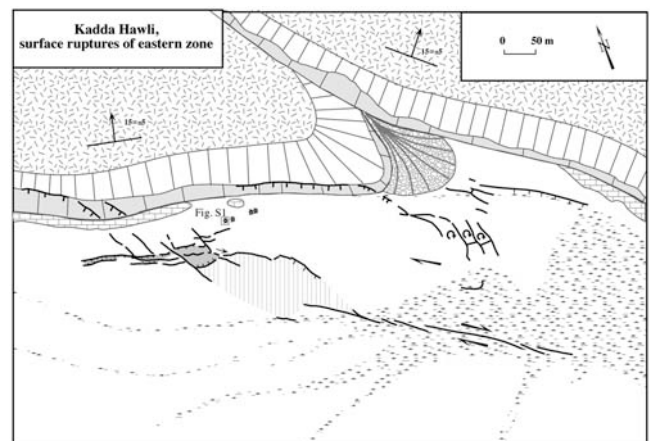


Figure B2. Detailed mapping of recent ruptures observed in areas 1, 2, 3, 6, 7, and 8.

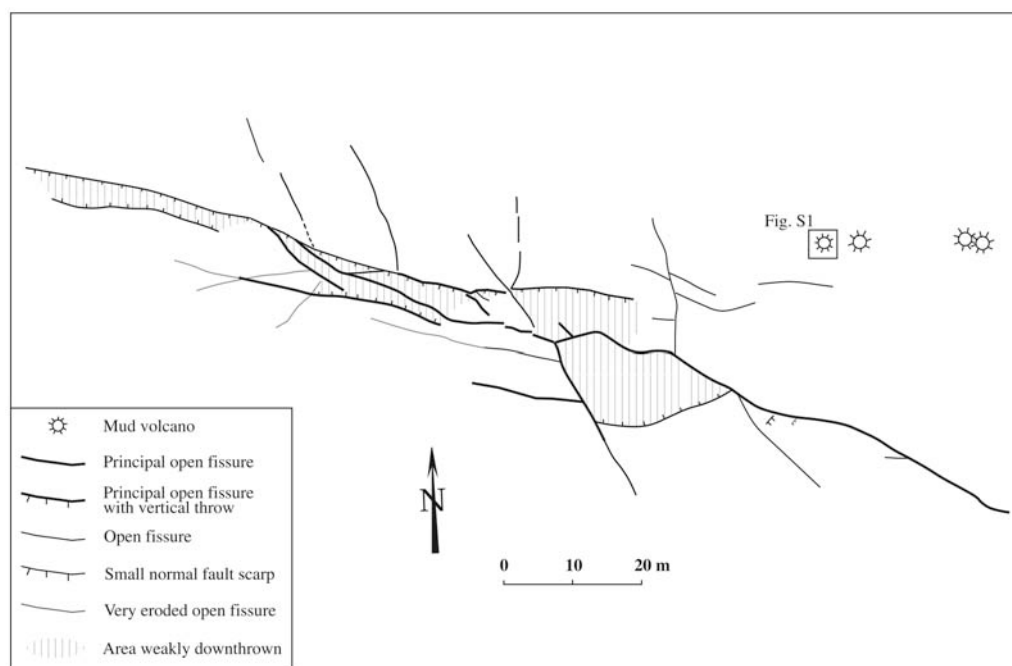


Figure B3. Map of surface ruptures in area 3 (small graben).

~5 km north of the Galafi ruptures. It is one of the numerous half-grabens formed by the ~N110°E-trending, second-order normal faults. The scarps of the second-order, south-southwest-dipping faults *F1* and *F2* bound the northeastern edge of this half-graben (Fig. 8) and delineate the sharp, southeastern wall of two tilted basaltic slices (*A* and *B*, Fig. 8). They strike N110°E and N125°E on average, respectively. A southwest-dipping, N140°E-striking third-order fault (*F3*) separates *A* and *B*. The tilted back of another block (*C*), cut by a third-order fault *f*, limits the southwestern edge of the half-graben, which drains toward the southeast.

Most of the breaks we mapped (~800 data points over an area ~1600 × 250 m², Fig. 8) are open fissures, several meters to 200-meters long, several centimeters to several

tens-of-centimeters wide and up to several meters deep. The most spectacular ones cut the flat sedimentary floor 100–350 m southwest of the cumulative *F1* and *F2* scarps and continue westward for ~900 m along the base of the *F1* free face or across its scree wedge (Fig. 8). A clear consequence of the 1989 earthquakes, such fissures in soft sediments will likely fill in, if not disappear, over the years.

In area 1 (box 1, Fig. 8), the floodplain is cut by half a dozen linear open fissures without detectable vertical throw, forming a dextral en échelon array about 430 m long, trending ~N120°E (Figs. 8 and B2). The two longest fissures strike N120°E and are ~125 and ~225 m long. Two others are 38 m and 58 m long, and the smallest one only 5 m long. They strike between N120°E and N130°E. Their opened

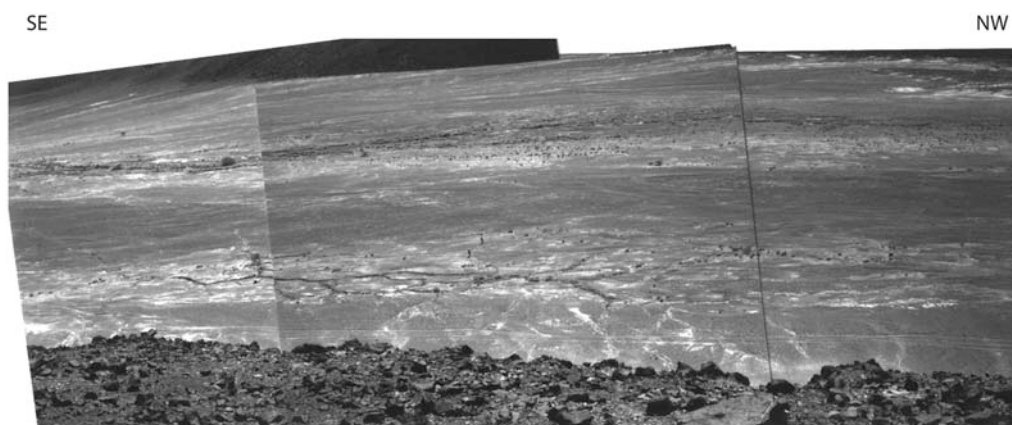


Figure B4. Overall, south-looking view of area 3 ruptures, from total-station base 1. Top of block *A* is in foreground. Note ruptures of area 1 on top left part of photograph.

width is up to 30 cm. The longest fissure is about 2 m deep. Some fissures may have been enlarged by water runoff. Farther east, in the continuation of the array, others may have been obliterated by recent flooding. The westernmost fissure connects areas 1 and 2.

The surface breaks in area 2 (box 2, Fig. 8) are fissures and normal scarplets striking either N110°–120°E or N140–150°E (Fig. B2). They delimit a rhomb-shaped zone, about 230 × 80 m² wide, which subsides slightly in its eastern part. The surface breaks in area 2 connect with those in areas 1 and 3.

In area 3 (Figs. B3 and B4), the rupture zone is ~250 × 60 m². We observe two main fissure sets. The first is composed of fissures striking N160°–180°E, 5–20 m long, several centimeters to tens-of-centimeters wide. The second set is composed of N80°–130°E-striking, open fissures, and normal eroded scarplets up to 12 cm high. Some open fissures have vertical throws several centimeters to tens-of-centimeters high. Some are up to 65 m long. The trends of the fissures showing the largest opening range between N100°E and N130°E. The small scarplets and the open fissures with vertical throws delimit a N105°E-trending, ~220 m-long, grabenlike structure, which widens from 5 m in the west to 35 m in the east. The principal fissures cross the central part of this small graben at a slight angle and tend to form a dextral en échelon array. The graben lies about 75 m south of the *F1* cumulative fault scarp. Area 3 seems connected to area 6 through eroded N80°–100°E-trending fissures and an alignment of mud-volcano craters (or sand-blows, ⊕ see Fig. S1 in the electronic supplement to this paper) 1–2 m in diameter. Areas 2 and 4 (Figs. 8 and B2) appear to be linked by the northernmost striking fissures in area 3, suggesting a dextral, rhomb-shaped transfer zone between the small graben in area 3 and the surface breaks in area 4.

In area 4 (Figs. 8 and B2), we mapped a rather continuous, 10–30 cm high, light-colored scarplet running across



Figure B5. North-northwest-looking view of faulted scree wedge along *F1* fault scarp, (middle of area 4). Light-colored scarplet across wedge, indicated by arrows, is coseismic 1989 rupture.

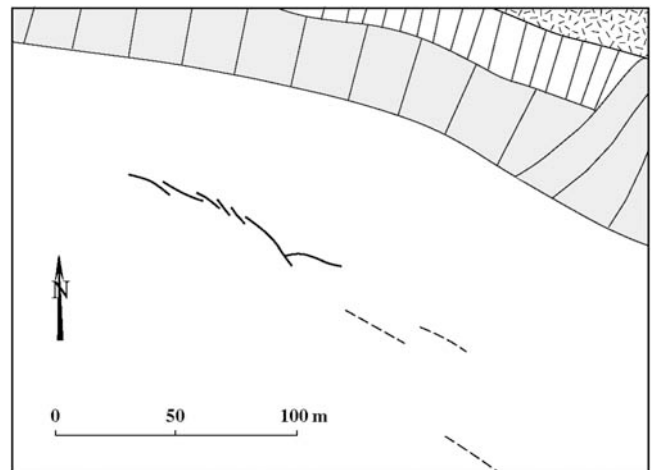


Figure B6. Map of ruptures in area 5 (most northwestern surface breaks of Kadda Hawli).

the scree wedge at the base of the *F1* cumulative scarp (Figs. 8 and B5). It either cuts the highest part of the scree wedge or marks contact between the free face and the scree,

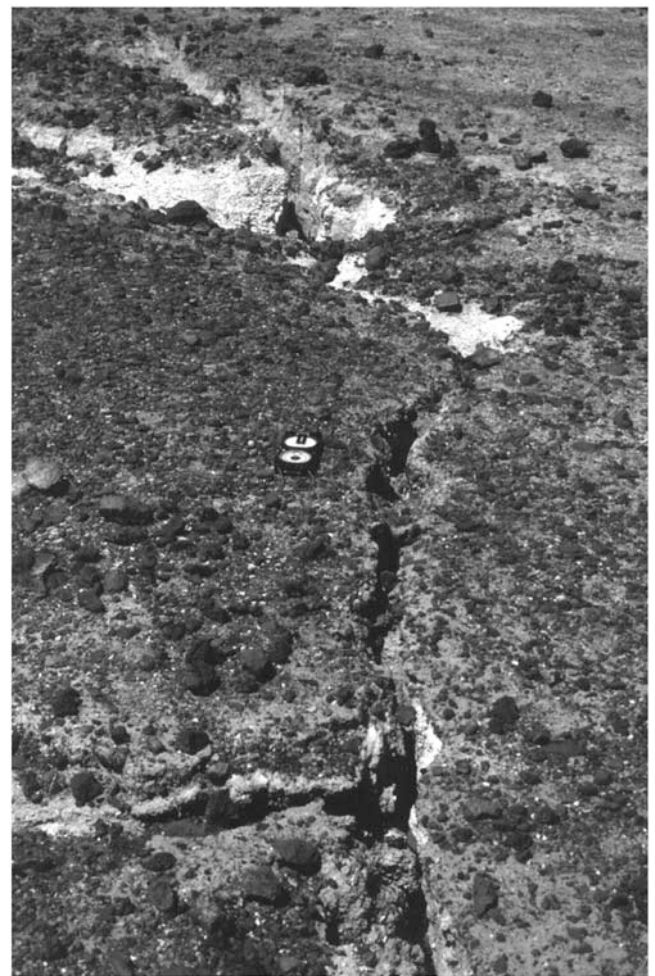


Figure B7. North-northwestward-looking closeup of open cracks in area 5 (compass gives scale).

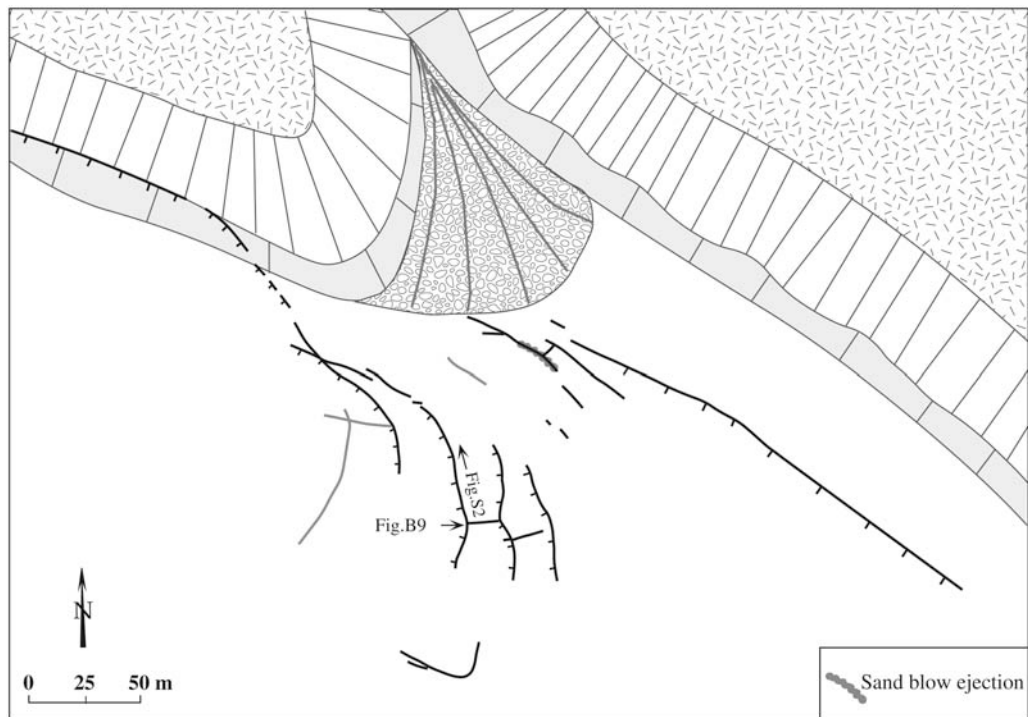


Figure B8. Map of surface ruptures in areas 7 and 8 (most southeastern breaks of Kadda Hawli).

as do most seismic ruptures in Afar (e.g., [Abdallah *et al.*, 1979](#); [Tapponnier *et al.*, 1990](#); [Manighetti, 1993](#); [Manighetti *et al.*, 2001](#)). It thus clearly formed due to slip on *F1* during the 1989 sequence. In the easternmost part of area 4, the scarplet curves and splits into N140°–150°E segments that obliquely crosscut the scree wedge downslope toward the small

graben observed in area 3 (Fig. 8). In the middle part of area 4, other N140°–150°E-trending scarplets cut across the scree wedge, suggesting they may have been connected to the now smoothed ruptures in the floodplain west of area 3. These scarplets form a dextral en échelon array along *F1*. No other seismic scarplet is visible westward on this fault.



Figure B9. East-looking view (location in Fig. B8) of fissures intersecting at high angles in area 7, cumulative fault scarp of *F2* in background.

In area 5 (Figs. 8 and B6), a patch of lacustrine calcareous sediments covered by a thin veneer of basaltic gravel is cut by ten open fissures ~10 cm wide (Fig. B7), 10–20 m long, striking $N130^\circ \pm 15^\circ E$, and located ~50 m southwest of the *F1* scarp base. These fissures form a dextral en échelon array along a mean $\sim N115^\circ E$ direction (Fig. B6). Those shown as dashed lines tend to form a left-lateral en échelon array along a mean $\sim N145^\circ E$ direction. West of area 5, we observed no further rupture. The gravel layer is thicker and coarser than elsewhere, however, making detection of surface breaks more difficult.

Area 6 shows an almost continuous, 10–30 cm high, light-colored scarplet running along the contact between the *F1* free face and its scree (Figs. 8 and B2). Just west of the alluvial fan that fills the *F1-F2-F3* intersection zone, the scarplet curves southeastward to continue into the graben floor. There, it gives place to open fissures with small vertical throws, which continue into area 7 (Fig. B8).

Area 7 (Figs. 8 and B8), downstream from the alluvial fan, shows the most unusual fissure network, measured with crosscutting, almost orthogonal open fissures (Fig. B9). The longer fissures (25–65 m long) strike $N160^\circ$ – $170^\circ E$. They are connected by shorter (7–15 m long) fissures. The easternmost fissure is filled, forming a shallow rill with regularly spaced tufts of grass. The other fissures are fresh, with sharp edges (⊕ Fig. S2 in the electronic supplement to this paper). They are 15–50 cm deep and have small, west-facing vertical throws. In the northwestern part of this area, the northerly striking fissures bend counterclockwise (Fig. B8) before merging with area 6 ruptures. Twenty-five meters to the south, a peculiar, open fissure exhibits an even sharper bend of more than 100° . All fissures but the southernmost one can be interpreted to form a dextral horse-tail termination at the eastern end of the *F1* seismic scarplet (area 6).

In area 8 (Figs. 8 and B8), open fissures cut through the lacustrine infill, downstream from the alluvial fan of site 6. They lie parallel to and 50 m south of the cumulative scarp of *F2*. Their strikes range between $N110^\circ E$ and $N125^\circ E$. They

are 5–20 cm wide. The easternmost and longest fissure is ~200 m long, with slight subsidence of the sediment floor to the south. The lengths of the others range between 20 m and 75 m. The westernmost fissures are located in the south-eastward continuation of *F3*. One of the fissures bears traces of sand and water ejection (Fig. B8). They form an overall dextral en échelon array with a mean trend of $N90^\circ E$, nearly parallel to *F1*. We could not find ruptures cutting across the alluvial fan, but they might be difficult to detect in coarse, loose pebbles.

Équipe de Tectonique
Institut de Physique du Globe de Paris
Sorbonne Paris Cité
UMR 7154 CNRS, France
(E.J., P.T., Y.G., J.C.R., R.A.)

Department of Earth Sciences
School of Earth and Planetary Sciences
Addis Ababa University
Ethiopia
(T.K.)

Géoazur—UMR 6526 CNRS
Université Nice Sophia Antipolis
Nice, France
(I.M.)

Université Pierre et Marie Curie
Université Paris 06
Institut des Sciences de la Terre de Paris
UMR 7193 CNRS
Paris, France
(B.M.)

UMR Isterre
Observatoire des Sciences de l'Univers de Grenoble
Maison des géosciences
Grenoble, France
(L.A.)

Manuscript received 9 October 2006